Inorganic Chemistry

pubs.acs.org/IC Article

Role of MCD and Mössbauer Spectroscopy in the Explanation of the Properties of a Highly Soluble (μ-Oxo)bis[tetra(*tert*-butyl)(phthalocyaninato)iron(III)] Complex, Its Pyridine Adduct, and Redox Forms Oxidized under Anaerobic Conditions in Non-Coordinating Solvents

Victor N. Nemykin,* Briana R. Schrage, Dustin E. Nevonen, Laurel A. Harrison, Kelly M. E. Newman, Vinod K. Paidi, and Johan van Lierop*

Cite This: *Inorg. Chem.* 2023, 62, 10203−10220 Read Online

ACCESS | Metrics & More | Article Recommendations | Supporting Information

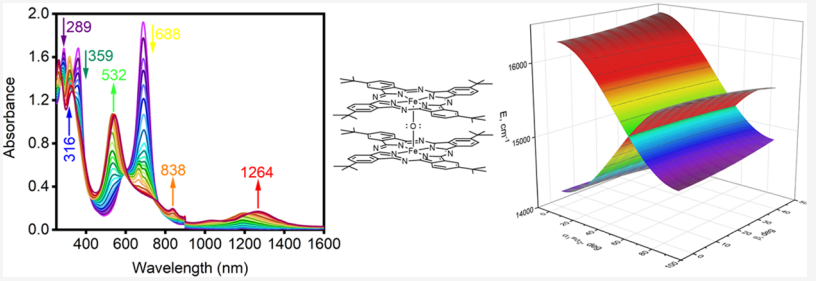

ABSTRACT: Solid-state Mössbauer spectra of a highly soluble (μ-oxo)bis[tetra(*tert*-butyl)(phthalocyaninato)iron(III)] complex **1** ($(Pc^{tBu}Fe)_2O$) consist of two doublets that represent bent geometry in μ-oxo(1) (**1a**, ΔE_Q = 0.43 mm/s, T = 10 K) and linear geometry in μ-oxo(2) (**1b**, ΔE_Q = 1.40 mm/s, T = 10 K) isomers with the ratio between two isomers depending on the purification method. Both isomers were found to be diamagnetic and transform entirely to the **1a** isomer in solution. The room- and low-temperature magnetic circular dichroism (MCD) spectra of **1a** μ-oxo(1) show one Faraday A- and one B-term between 670 and 720 nm, which correlate with the 690 nm band and 709 nm shoulder observed in the UV−vis spectrum of this compound. UV−vis and MCD spectra of **1a** are almost independent of the temperature. Both **1a** and **1b** are diamagnetic between room temperature and 4 K. Electrochemical experiments show up to three oxidations and up to four reduction processes in **1a**. Its oxidation under spectroelectrochemical or chemical (in the absence of oxygen-containing oxidants) conditions in non-coordinating solvents results in the formation of broad NIR bands around 1195 nm (first oxidation) and 1264 nm (second oxidation). The MCD spectra of the redox-active species show a Faraday B-term signal with negative amplitude in this region and are very different from those in the monomeric $Pc^{tBu}(1-)Fe^{III}X_2$ complexes **5X** (X = Cl^- or $CF_3CO_2^-$). The pyridine adduct of **1a** ($(PyPc^{tBu}Fe)_2O$; **2Py**) is paramagnetic (μ_B = 2.19, g = 2.11, and J = −6.1 cm^{-1}) and has a major peak at 627 nm of its UV−vis spectrum, which is associated with a MCD pseudo A-term. Density functional theory (DFT) and time-dependent DFT (TDDFT) calculations, along with the exciton coupling theory, were used to explain the unusually red-shifted intense transitions in **1a** as well as the H-aggregate-like spectra of the pyridine adduct **2Py**.

INTRODUCTION

Rich coordination chemistry, coupled with easy access to different oxidation and spin states of iron porphyrins and their analogues such as phthalocyanines, is responsible for a large interest in these compounds.[1−18] Iron complexes of phthalocyanines are among the most effective systems involved in the catalytic oxidation of a variety of organic substrates such as alkanes, alkenes, aromatic hydrocarbons, and phenols because of their high chemical and thermal stabilities as well as relatively low cost.[5] The catalytic activity of iron phthalocyanine (PcFe) and its substituted analogues ($Pc^{Rn}Fe$) (R is a substituent and n = 4 or 8) in chemical, electrochemical, and photochemical reactions is well documented.[5,19−26] Moreover, as it was shown recently by several research groups, iron phthalocyanine dimers of general formula

Received: March 18, 2023
Published: June 22, 2023

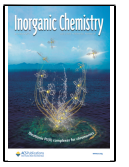

https://doi.org/10.1021/acs.inorgchem.3c00897
Inorg. Chem. 2023, 62, 10203−10220

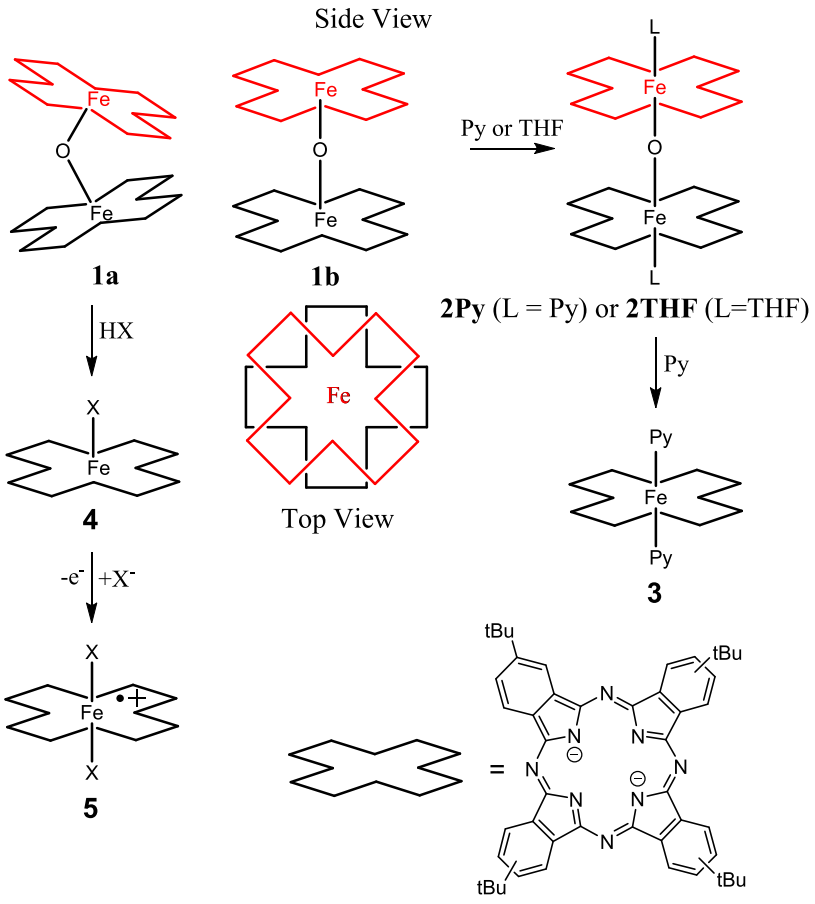

Figure 1. General reaction scheme with labeling conventions.

$(Pc^{Rn}Fe)_2X$ (X = O or N) can also catalyze numerous oxidation reactions of organic substrates.[27−39] More importantly, it was demonstrated that the $(Pc^{Rn}Fe)_2N$ dimer can catalyze the oxidation of methane at mild conditions.[40,41] The parent $(PcFe)_2O$ complex has been known for several decades and, depending on the purification method, can form bent μ-oxo(1) and linear μ-oxo(2) isomers (with respect to the Fe−O−Fe angle, Figure 1) that have different Mössbauer parameters and magnetic properties.[6,42−53] However, purification and characterization of these isomers (and thus, verification of their magnetic properties) is hindered by the low solubility of the $(PcFe)_2O$ complex in common organic solvents. Peripheral functionalization of the $(PcFe)_2O$ complex leads to the formation of highly soluble derivatives of general formula $(Pc^{Rn}Fe)_2O$ (n = 4 or 8)[54,55] that were shown to catalyze a variety of oxidation reactions under homogeneous conditions.[27−30] Unlike unsubstituted μ-oxo(1) and μ-oxo(2) isomers, based on the earlier reports by Lukyanets and co-workers[55] as well as Hanack and co-workers,[54] it seems that soluble derivatives of the $(PcFe)_2O$ complex are diamagnetic at room temperature. Moreover, their redox properties as well as spectroscopic signatures of the redox-active species generated under anaerobic conditions in the absence of coordinating solvents have never been explored. Before discussing the catalytic reaction mechanism that involves the $(Pc^{tBu}Fe)_2O$ complex in the next report, the following questions will be addressed in this paper: (i) Why do the UV−vis spectra of the parent and functionalized $(Pc^{Rn}Fe)_2O$ complexes have a red-shifted Q-band while all other similar phthalocyanine μ-oxo dimers possess a blue-shifted Q-band? (ii) Why are the UV−vis spectra of μ-oxo(1) and μ-oxo(2) isomers the same while their Mössbauer spectra are different? (iii) What are the magnetic properties of μ-oxo(1) (**1a**) and μ-oxo(2) (**1b**) forms as well as their axially coordinated $(PyPc^{tBu}Fe)_2O$ counterpart (**2Py**)? (iv) What are the spectroscopic signatures of the species oxidized under anaerobic conditions obtained by the oxidation of the $(Pc^{tBu}Fe)_2O$ core in non-coordinating solvents?

RESULTS

Spectroscopy, Electrochemistry, and Spectroelectrochemistry. The (μ-oxo)bis[tetra(*tert*-butyl)(phthalocyaninato)iron(III)] complex (**1**)[54,55] was chosen as a platform for the current investigation (Figure 1) as the presence of eight *tert*-butyl groups in the system dramatically increases its solubility in common organic solvents and decreases the tendency toward aggregation, which is well-known for phthalocyanines.[1] Depending on the preparation and purification protocols, the Mössbauer spectra of **1** consist of a different ratio of μ-oxo(1) and μ-oxo(2) isomers (labeled below as **1a** and **1b**, respectively; see Figures 2 and S1 and Table 1). In the case when the metalation reaction on metal-free phthalocyanine was conducted in *N*,*N*-dimethylaminoethanol, **1b** isomer would dominate as the reaction product (as determined by Mössbauer spectroscopy; see Figure 2). However, when complex **1** was prepared from 4-*tert*-butylphthalonitrile without the solvent or in nonpolar aromatic high boiling point solvent (*o*-dichlorobenzene (*o*-DCB) or 1-chloronaphthalene), **1a** isomer would dominate as the reaction

https://doi.org/10.1021/acs.inorgchem.3c00897
Inorg. Chem. 2023, 62, 10203−10220

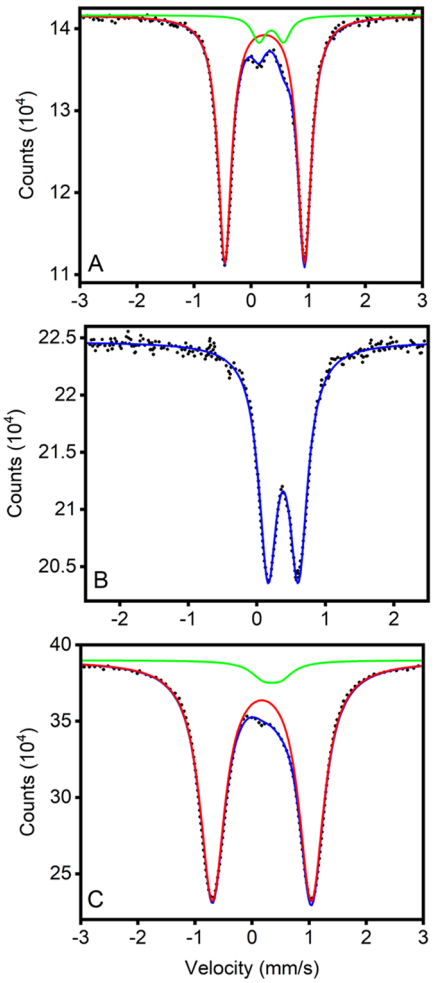

Figure 2. Mössbauer spectra of solid-state **1** (mixture of **1a** and **1b**, (A); 10 K); frozen toluene solution of the same sample of **1** (effectively **1a**, (B); 50 K); frozen solution of **1** after the addition of 10 μL of pyridine (**2Py**, (C); 10 K). All spectra are referenced to α-Fe. Red and green lines represent the individual doublet components. Blue line is a cumulative line for the simulated spectra.

product (as determined by Mössbauer spectroscopy; see Figure S1). As indicated in Table 1, the ratio differs between 9:91 and 51:49 (**1a**/**1b**), and a similar simultaneous presence of both **1a** and **1b** was also observed earlier by Hanack and co-workers[1] for this compound and the other substituted analogues of general formula $(Pc^{Rn}Fe)_2O$ (n = 4 or 8).[54]

Superconducting quantum interference device (SQUID) magnetometry data are suggestive that all samples of **1** (independent of the **1a**/**1b** ratio) are diamagnetic between 4 K and room temperature. No electron paramagnetic resonance (EPR) signal was found for **1** at room temperature or 77 K in toluene. As expected, the ^{1}H NMR spectrum of the starting complex **1** resembles the spectrum of regular diamagnetic tetrasubstituted phthalocyanines and is in accord with the existence of this compound as a mixture of all possible positional isomers, which is in good agreement with the previously reported data on this compound.[54,55]

The room-temperature UV−vis spectrum of **1** in toluene is shown in Figure 3 and consists of a high-intensity Q-band observed at 688 nm with a prominent shoulder at 712 nm and a B-band at 363 nm followed by a band at 312 nm. The spectrum shape remains the same in all non-coordinating

Table 1. Mössbauer Parameters for Selected Iron(III) Phthalocyanine μ-Oxo Dimers and $Pc^{Rn}(1-)FeCl_2$

compound	T, K	δ, mm/s[a]	ΔE_Q, mm/s	ref
$(Pc^{tBu}Fe)_2O$ μ-oxo(1), **1a**	290	0.24	0.46	this work (tw), solid
$(Pc^{tBu}Fe)_2O$ μ-oxo(1), **1a**	77	0.34	0.41	tw, toluene
$(Pc^{tBu}Fe)_2O$ μ-oxo(1), **1a**	50	0.38	0.44	tw, toluene
$(Pc^{tBu}Fe)_2O$ μ-oxo(1), **1a**	10	0.33	0.48	tw, solid
$(Pc^{tBu}Fe)_2O$ μ-oxo(2), **1b**	290	0.15	1.38	tw, solid
$(Pc^{tBu}Fe)_2O$ μ-oxo(2), **1b**	10	0.24	1.40	tw, solid
$(Pc^{tBu}Fe)_2O$ μ-oxo(2), **1b**	293	0.13	1.31	54, solid
$(Pc^{tBu}Fe)_2O$ μ-oxo(2), **1b**	90	0.22	1.38	54, solid
$(PcFe)_2O$ μ-oxo(1)	295	0.25	0.42	6, 47, solid
$(PcFe)_2O$ μ-oxo(1)	77	0.36	0.44	47, 51, solid
$(PcFe)_2O$ μ-oxo(1)	4.2	0.37	0.44	6, 47, solid
$(PcFe)_2O$ μ-oxo(2)	295	0.18	1.05	56, solid
$(PcFe)_2O$ μ-oxo(2)	77	0.25	1.26	56, solid
$(PcFe)_2O$ μ-oxo(2)	4.2	0.26	1.25	56, solid
$[(Py)Pc^{tBu}Fe]_2O$, **2Py**	10	0.17	1.74	tw, Py
$[(Py)PcFe]_2O$	4.2	0.18	1.73	57, solid
$[(4\text{-MePy})PcFe]_2O$	295	0.12	1.81	57, solid
$[(4\text{-MePy})PcFe]_2O$	77	0.19	1.75	57, solid
$[(4\text{-MePy})PcFe]_2O$	4.2	0.20	1.76	57, solid
$[(Pip)PcFe]_2O$	4.2	0.19	1.61	57, solid
$[(1\text{-MeIm})PcFe]_2O$	4.2	0.17	1.58	57, solid
$Pc^{tBu}(1-)FeCl_2$	293	0.17	2.39	tw, solid
$Pc^{tBu}(1-)FeCl_2$	88	0.25	2.45	tw, solid
$Pc(1-)FeCl_2$	?	0.35 no ref	2.15	58, 59, solid
$Pc(1-)FeCl_2$	77	0.20	2.57	60, solid

[a]All isomer shifts are referenced to α-Fe.

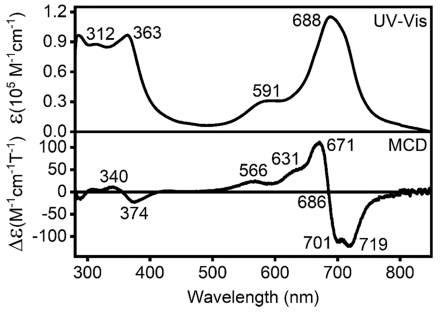

Figure 3. Room-temperature UV−vis and MCD spectra of **1** in toluene.

solvents, i.e. benzene, toluene, hexane, chloroform, 1,2-dichlorobenzene (o-DCB), and dichloromethane without any appreciable solvatochromic behavior. Overall, the UV−vis spectrum of **1** closely resembles those reported for the unsubstituted $(PcFe)_2O$[6] and substituted $(Pc^{Rn}Fe)_2O$ compounds.[54] Both Q- and B-bands in **1** correlate with the Faraday A-terms in the magnetic circular dichroism (MCD) spectrum of **1** centered at 686 and 359 nm, respectively (Figure 3), while the prominent shoulder observed at 712 nm in the UV−vis spectrum of **1** correlates with the Faraday MCD B-term at 719 nm. The shape of the UV−vis spectrum does not change significantly over the +20 to −55 °C temperature range (Figure S2). Similarly, the low-temperature MCD spectrum of **1** has the same shape as the room-temperature spectrum, although the visibility of the low-energy B-term significantly

https://doi.org/10.1021/acs.inorgchem.3c00897
Inorg. Chem. 2023, 62, 10203−10220

improves (Figure S3). The lack of change of the MCD spectral profile between room temperature and 200 K is indicative of the diamagnetic ground state in complex **1**, which is a result of strong antiferromagnetic coupling between two high-spin (s = 5/2−5/2) iron(III) centers. This agrees with the NMR and magnetochemistry data. Similar to magnesium or zinc phthalocyanine cation radicals,[61−64] it also suggests that the MCD spectra of **1** can be described using Faraday A- and B-terms. This is in stark contrast to the earlier reported (by Stillman and co-authors) MCD spectra of $[Pc(2-)Fe^{III}(CN)_2]^-$[65] and $Pc(1-)Fe^{III}Cl_2$[66] complexes that have a strong temperature dependence and were described using MCD C-terms. ^{1}H NMR, UV−vis, and MCD spectra of complex **1** recorded for samples with different ratios of **1a** and **1b** were found to be identical. If one assumes that **1a** has bent and **1b** has linear geometries, as suggested earlier for the unsubstituted $(PcFe)_2O$ complex,[6,56] different UV−vis and MCD spectra should be expected, which is not the case. In order to resolve this controversy, we have recorded Mössbauer spectra of different samples in frozen toluene (Figures 2 and S1). We found that, independent of the initial **1a**/**1b** ratio observed in the solid state, only the **1a** isomer is observable in a frozen solution. According to density functional theory (DFT) calculations discussed below, the bent structure of **1a** is energetically slightly more stable than the linear structure of **1b**. Thus, it is not surprising to see that the linear **1b** in solution transforms to the bent **1a**, and the UV−vis, MCD, and NMR spectra of **1** in solution are reflective of the **1a** isomer.

Titration of toluene or hexane solution of **1a** with pyridine leads to the transformation of its initial Q-band around 690 nm into a new band centered at 626 (toluene) or 621 nm (hexane) (Figure 4). This transformation correlates well with the

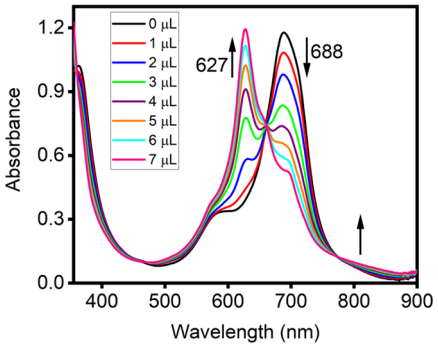

Figure 4. Transformation of **1a** into **2Py** in toluene solution.

previous observations of Lukyanets and co-workers[54] as well as Hanack and co-workers[55] on **1a**. It is also consistent with similar data on the parent $(PcFe)_2O$[57] and is reflective of axial coordination of two pyridine molecules to **1a** with the formation of **2Py** (Figure 1). Solutions of **2Py** undergo a slow transformation to $PcFe^{II}Py_2$ complex **3** (which can be easily monitored by the appearance of the intense Q-band at 660 nm and metal-to-ligand charge transfer (MLCT) band at 414 nm, Figure S11).[67−69] The transformation in the toluene/pyridine system is completed in few hours and a similar timescale for the unsubstituted $(PyPcFe)_2O$ complex was reported by Ercolani and co-workers.[70,72,73] The rate of such a transformation depends on the concentration of pyridine and polarity of the solvent. Taking into consideration the transformation of **2Py** to **3** and the typical timeframe for an MCD experiment, it is difficult to record a pure MCD spectrum of **2Py** that will not be contaminated by a small amount of **3**. Nevertheless, from the MCD spectra of **2Py** (Figure 5), it is clear that the most intense band between 620

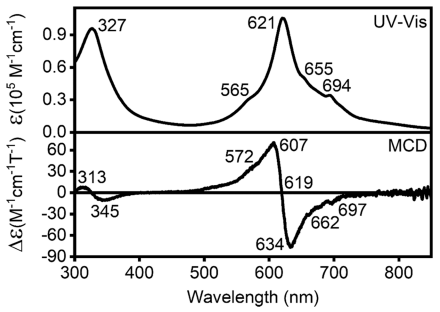

Figure 5. UV−vis and MCD spectra of **2Py** in hexane. The shoulder at 655 nm in the UV−vis spectrum and the signal at 662 nm in the MCD spectrum belong to the $PcFePy_2$ complex slowly formed from **2Py** (Figure 1).

and 630 nm is associated with the MCD pseudo A-term like signal and the weak band around 695 nm is associated with an MCD B-term. The Soret band in **2Py** is observed at 327−330 nm and is associated with another MCD pseudo A-term. Although **2Py** is not stable in solution for a prolonged time, it can be isolated in an almost pure form in the solid state.[57] Indeed, fast evaporation of the reaction media results in the formation of the sample that consists of 94% **2Py** and only 6% of the starting diamagnetic **1a**. The Mössbauer spectrum of this sample (Figure 2C) has a characteristic (for the low-spin (s = 1/2) hexa-coordinated Fe(III)) doublet[57] with parameters shown in Table 1. The magnetometry data on **2Py** are shown in Figure 6 and are suggestive of the formation of the weakly antiferromagnetically coupled Fe(III)−O−Fe(III) (s = 1/2 − s = 1/2) species. The fitting parameters (using a spin Hamiltonian with the PHI code) give the room-temperature value of the magnetic moment of μ_B = 2.19 and g = 2.11. The antiferromagnetic exchange constant J is −6.1 cm^{-1}. These values are in good agreement with the data reported by

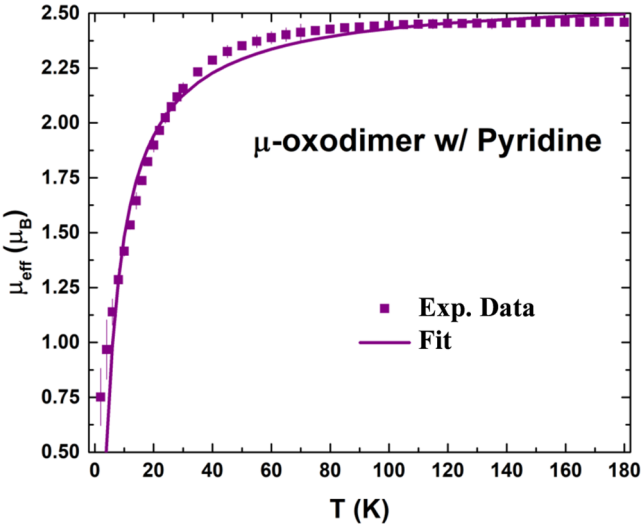

Figure 6. Magnetic moment of **2Py** as a function of temperature. PHI program[71] was used for modeling of the coupling in **2Py** (see Experimental Section for details).

https://doi.org/10.1021/acs.inorgchem.3c00897
Inorg. Chem. 2023, 62, 10203−10220

Ercolani and co-workers on the low-spin antiferromagnetically coupled unsubstituted $(LPcFe)_2O$ complexes (L is organic amine or N-heterocycle; μ_B = 1.86−2.16; and J = −5.5 to −6.3 cm^{-1}).[57] The ultimate structure of these compounds was also previously reported for the unsubstituted analogue by Ercolani and co-authors (the X-ray structure of $[(1\text{-MeIm})PcFe]_2O$).[70]

The redox properties of $(PyPcFe)_2O$ were studied by Ercolani and co-workers in pyridine,[72] while the electrochemical behavior of the parent $(PcFe)_2O$ has not been evaluated because of its low solubility in nonpolar solvents. On the contrary, the high solubility of **1a** in common organic solvents allowed us to study its redox properties in two noncoordinating solvents (dichloromethane (DCM) and *o*-DCB) using either 0.1 M tetrabutylammonium perchlorate (TBAP) or 0.05 M tetrabutylammonium tetrakis(pentafluorophenyl)-borate (TFAB) as the supporting electrolyte. The latter electrolyte is known for its low ion-pairing strength, which allows better separation between the oxidation waves.[68] First, we found that the influence of the supporting electrolyte on the observed redox processes in **1a** is rather small (Figure 7 and Table 2).

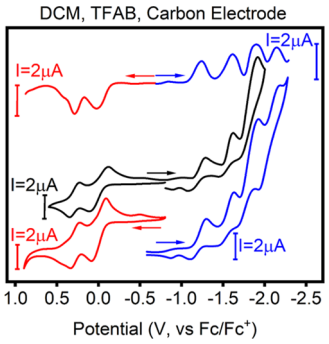

Figure 7. Cyclic voltammetry (CV) and differential pulse voltammetry (DPV) data for **1a** in the DCM/0.05 M TFAB system at room temperature. Red and blue lines represent individual oxidative and reductive scans, respectively. Black line represents a cumulative CV.

For instance, in both DCM/0.1 M TBAP and DCM/0.05 M TBAF systems, three oxidation and four reduction processes were observed. The first two oxidation processes are reversible and separated by 320 (DCM/0.1 M TBAP) or 290 (DCM/0.05 M TFAB) mV. Such nearly constant separation between the Ox1 and Ox2 processes is rather surprising as one might expect that such a separation will be significantly larger for the TBAF electrolyte due to its low ion-pairing ability. The third oxidation process in DCM is irreversible. Out of four observed reduction processes in **1a**, only the first reduction process is reversible (Figure 7). In a *o*-DCB/0.1 M TBAP system, two reversible oxidation processes were observed, while out of three reductions, only the last process is irreversible (Table 2). The electrochemistry of **2Py** in Py/0.1 M TBAP correlates well with the previous report by Ercolani and co-workers on the unsubstituted $(PyPcFe)_2O$ complex.[72] In particular, two oxidation processes at +0.43 and +0.83 V correlate well with the earlier reported oxidation potentials (Table 2), while the smaller oxidation wave observed at +0.64 V can be attributed to the first oxidation process in the $PcFePy_2$ (**3**) complex, which slowly forms during the transformation of **2Py** into **3** during the electrochemical experiment.[73] In addition, two reduction processes were observed at −0.73 and −1.16 V, while the third process has a significantly larger current that Ercolani attributed to the transformation of the dimeric structure into the monomeric one.[72] Based on the recent crystallographic structure of the PyPcFe−O−FePc(THF) complex,[74] one might expect that the dissolvation of **1a** in tetrahydrofuran (THF) will result in the formation of **2THF** (Figure 1). The electrochemical data on **2THF** is indicative of three oxidation processes (with the first process being reversible) along with three irreversible reduction processes (Figure S4) with the potentials shown in Table 2.

The stepwise oxidation of **1a** under spectroelectrochemical conditions in a DCM/0.15 M TFAB system is shown in Figure 8. During the first oxidation process, the Q- and B-bands at

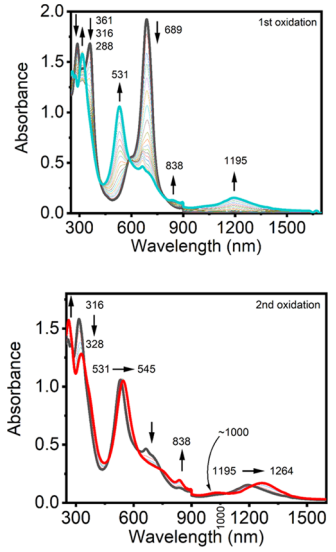

Figure 8. First (top) and second (bottom) oxidation of **1a** under spectroelectrochemical conditions in a DCM/0.3 M TBAP system.

Table 2. Redox Potentials for Oxidation and Reduction Processes in Iron(III) Phthalocyanine μ-Oxo Dimers[a]

complex	solv.	electr.[b]	Ox3	Ox2	Ox1	R1	R2	R3	R4	ref[c]
$(Pc^{tBu}Fe)_2O$ μ-oxo(1), **1a**	DCM	TFAB		1.03	0.74	−0.45	−0.80	−1.06	−1.31	tw
	DCM	TBAP	1.82[irr]	1.13	0.81	−0.60	−0.97	−1.21	−1.41	tw
	o-DCB	TBAP		1.05	0.65	−0.80	−1.14	−1.43		tw
	THF	TBAP	1.31	0.99	0.73	−0.54	−0.94	−1.34		
$[(Py)Pc^{tBu}Fe]_2O$, **2Py**	Py	TBAP		0.83	0.43	−0.73	−1.16	−1.47[irr]		tw
$[(Py)PcFe]_2O$	Py	TBAP		0.87	0.47	−0.59	−0.95			72, 73

[a]All potentials reported in this table are versus saturated calomel electrode (SCE). [b]Electrolyte. 0.1 M TBAP or 0.05 M TFAB were used in the experiments. [c]tw = this work.

https://doi.org/10.1021/acs.inorgchem.3c00897
Inorg. Chem. 2023, 62, 10203−10220

688 and 359 nm, respectively, lose their intensity, while new bands at 316, 532, 838, and 1195 nm appear in the spectra. One might assume that the low-energy band observed at 1195 nm in $[\mathbf{1a}]^{+\bullet}$ represents the intervalence charge-transfer (IVCT) transition between the one-electron oxidized and neutral phthalocyanine ligands.[75−77] However, the spectroscopic signatures for the second oxidation process questioned this assignment. Indeed, during the second oxidation process, the low-energy band at 1195 nm undergoes a red shift to 1264 nm, the initial band at 531 nm shifts to 545 nm, and the band at 316 nm transforms into a transition at 328 nm. The new bands observed in $[\mathbf{1a}]^{2+}$ at ∼840 and ∼1000 nm correlate well with the UV−vis spectrum of $[Pc^{tBu}Zn]_2^{2+}$ species.[61] A significant change in the absorption profile between **1a** and $[\mathbf{1a}]^{+}/[\mathbf{1a}]^{2+}$ is indicative of oxidation of the phthalocyanine macrocycle rather than iron(III) ion oxidation; however, the accurate assignment of the low-energy near-infrared (NIR) band will require further investigation.

Overall, the two-electron oxidation process is ∼90% reversible. Indeed, the oxidized $[\mathbf{1a}]^{2+}$ species can be reduced back to the initial μ-oxo dimer **1a** under spectroelectrochemical conditions with ∼90% yield (Figure S5). A similar transformation of **1a** was observed in a *o*-DCB/0.3 M TBAP system. We were able to chemically oxidize **1a** to $[\mathbf{1a}]^{+}$ using AgOTf as an oxidant with the final UV−vis and MCD data shown in Figure 9. No further oxidation of $[\mathbf{1a}]^{+}$ to $[\mathbf{1a}]^{2+}$ was

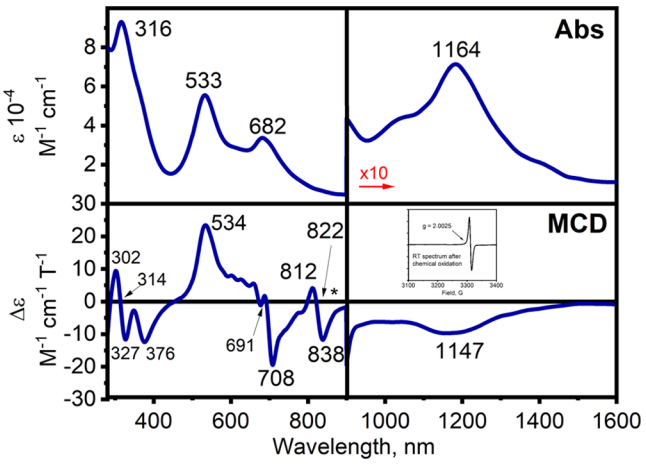

Figure 9. UV−vis and MCD spectra of $[\mathbf{1a}]^{+\bullet}$ in DCM.

observed and we failed to find a different oxidant that can reproducibly accommodate this transformation. Similar to the double-decker lanthanide phthalocyanines of general formula Pc_2Ln, the low-energy band observed in the 1000−1700 nm region is associated with the MCD B-term of negative intensity, while the 533 nm band is associated with the MCD B-term of positive intensity.[78] However, in the case of neutral Pc_2Ln complexes, the low-energy band in the 1000−1700 nm region was assigned as an IVCT transition between the Pc(2−) and Pc(1−) ligands, which may or may not be the case for $[\mathbf{1a}]^{+}$. The MCD pseudo C-term observed at 822 nm was attributed to a small monomeric impurity originating from the $Pc^{tBu}(1-)FeCl_2$ complex (**5Cl**) with a phthalocyanine cation-radical (the MCD spectra of the unsubstituted analogue of **5Cl** were described by Stillman and Ough).[66] Indeed, when green $Pc^{tBu}FeCl$ **4Cl** (obtained by the reaction of **1a** and HCl vapors) was oxidized under spectroelectrochemical conditions, it formed the red **5Cl** complex, which has characteristic bands at 535 and 838 nm (Figure 10). A similar transformation was observed upon the chemical oxidation of **4TFA** (formed by the

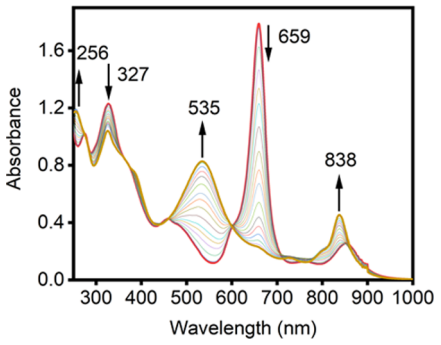

Figure 10. Oxidation of **4Cl** to **5Cl** under spectroelectrochemical conditions in the DCM/0.3 M TBAP system.

treatment of **1a** with trifluoroacetic acid (TFA)). The MCD spectra of **5Cl** and **5TFA** are shown in Figures 11 and S6.

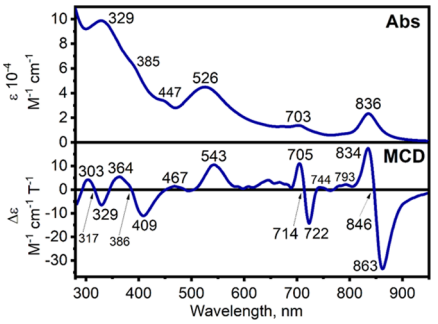

Figure 11. UV−vis and MCD spectrum of **5Cl** in DCM.

Our results discussed above are very similar to UV−vis and MCD spectra of the $[Pc(1-)Fe^{III}Cl_2]$ complex reported earlier by Stillman and Ough.[66] In particular, the low-energy band at 836 nm in **5Cl** is associated with the strong temperature-dependent MCD C-term, while the transition at 526 nm is associated with the MCD B-term of positive amplitude. Their room-temperature and 88 K Mössbauer spectra of **5Cl** are very close to those observed for our unsubstituted phthalocyanine analogue $[Pc(1-)Fe^{III}Cl_2]$ complex (Table 1 and Figure S7). The 77 K EPR spectrum of the $[\mathbf{1a}]^{+}$ complex has a characteristic (for the phthalocyanine cation radical) signal with a g = 2.00 value (Figure 9). A similar free-radical signal was recently observed by Kenney and co-workers upon single-electron oxidation of the $(RO\text{-}PcSi)_2O$ dimer.[79] However, although such a signal can be explained by the formation of the $[Pc(2-)Fe^{III}\text{-}O\text{-}Pc(1-)Fe^{III}]^{+}$ complex with two strongly antiferromagnetically coupled s = 5/2−5/2 Fe(III) centers, we cannot be absolutely sure that this signal reflects the formation of $[\mathbf{1a}]^{+}$ as the minor degradation of phthalocyanine ligand can also give a similar spectroscopic signature at this temperature. The lack of Fe(IV) centers in $[\mathbf{1a}]^{+\bullet}$ was further confirmed by its Mössbauer spectrum (Figure S12). Although because of a week-long transportation, this sample is contaminated with the degradation product, no characteristic for Fe(IV) doublets with low (∼−0.1 to 0.0 mm/s) isomer shift was observed in the spectrum. The first oxidation process under spectroelectrochemical conditions for **2THF** is shown in Figure S8. The initial UV−vis spectrum has three major low-

https://doi.org/10.1021/acs.inorgchem.3c00897
Inorg. Chem. 2023, 62, 10203−10220

energy peaks observed at 695, 659, and 626 nm. The 695 band corresponds to the initial **1a** in THF, while the band at 626 reflects the formation of the **2THF** complex. Thus, the UV−vis spectrum of **1a** in THF in the presence of 0.3 M TBAP is reflective of **1a** ⇋ "**X**" ⇋ **2THF** equilibrium in which species "**X**" has an unknown nature (potentially (THF)PcFe-O-PcFe complex). Nevertheless, oxidation of these species under spectroelectrochemical conditions is reversible and results in the formation of a 529 nm band, which is similar to that observed in $[\mathbf{1a}]^{+\bullet}$.

DFT and Time-Dependent DFT (TDDFT) Calculations. In order to further elucidate the electronic structures of **1a** and **1b** and elaborate on the optical and magnetooptical properties of dimers **1a**, **1b**, and **2Py**, we have conducted density functional theory (DFT) and time-dependent DFT (TDDFT) calculations on these compounds. The choice of the exchange-correlation functional (ECF) used in calculations is discussed in detail in the Supporting Information and is based on the requirements expected for phthalocyanine μ-oxo dimers and double-decker Pc_2Ln and $[Pc_2Ln]^-$ complexes.[80−84] For the **1a** and **1b** complexes, geometry optimizations with the HISSbPBE ECF suggest that the lowest energies correspond to the broken-symmetry calculations in which two $s = 5/2$ iron(III) centers are antiferromagnetically coupled via the μ-oxo bridging atom. The high-spin and open-shell calculations result in significantly higher-energy structures, which agrees well with the diamagnetism of **1a** and **1b** (Table S2). This correlates well with the previous report by Sorokin and co-authors on **1b**.[35,39] However, in our hands, frequency calculations reveal that the linear **1b** structure is not a local minimum for all four ECFs mentioned above. The single negative DFT-predicted frequency associated with the linear structure **1b** transforms it into bent **1a**. The DFT-predicted energy difference between **1a** and **1b** is only 0.72 kcal/mol for the HISSbPBE ECF. Such a small difference is within the range for crystal packing forces (and/or additional dispersion forces caused by peripheral *tert*-butyl groups) and can explain why the linear structure **1b** can be stabilized in the solid state but not in solution. DFT-predicted geometries for **1a** and **1b** have iron centers pushed away from the phthalocyanine plane toward the oxygen atom. The bent structure of **1a** has phthalocyanine ligands in a staggered conformation and the lowest energy structure of linear **1b** has two phthalocyanine ligands close to the staggered conformation. Contrary to dimers **1a** and **1b**, geometry optimization with the HISSbPBE ECF on dimer **2Py** converges only to linear geometry, which agrees well with the experimental spectroscopy, magnetochemistry, and X-ray crystallography.[70] Moreover, in agreement with the magnetic susceptibility data, the energy of the paramagnetic triplet state formed by two low-spin iron(III) centers is lower than the energies of the antiferromagnetically coupled diamagnetic state or open-shell singlet (Table S2). The iron centers were predicted to be close to the in-plane geometry, and two phthalocyanine ligands are located in a staggered conformation. The antiferromagnetic coupling constant for **1a** (-97 cm^{-1}) was predicted to be significantly larger than that in **2Py** (-14 cm^{-1}), which, on the qualitative level, agrees with the experimental data. The DFT-predicted Mössbauer quadrupole splittings for **1a** (0.47 mm/s) and **2Py** (1.92 mm/s) are also in good agreement with the experimental data (Table 1).

With reasonable geometries of dimers **1a** and **2Py** in hand, we ran an array of TDDFT calculations on these systems using wB97X ECF (see the Supporting Information for details). The choice of this long-range corrected ECF is not surprising as one might expect that both $\pi \rightarrow \pi^*$ and charge-transfer (CT) transitions should play a significant role in the nature of the excited states in **1a** and **2Py**. The DFT-predicted energy diagrams for **1a** and **2Py** are shown in Figure 12, while the

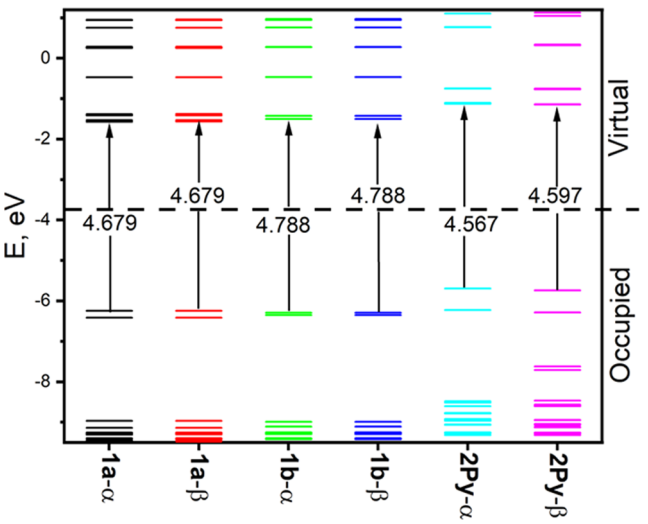

Figure 12. DFT-predicted energy diagram for **1a**, **1b**, and **2Py**.

compositions of the frontier orbitals are outlined in Figure 13. The MO isosurfaces for the frontier orbitals are shown in Figures 14 and S9. The total DFT-predicted spin densities for the lowest energy structures of **1a** and **2Py** are shown in Figure S10 and are reflective of anti- (**1a**) and ferromagnetic (**2Py**) coupling in these systems.

The TDDFT-predicted UV−vis spectra of **1a** and **2Py** in comparison with the experimental data are shown in Figure 15. The data for both compounds correlate well with the experimental data. In the case of bent dimer **1a**, TDDFT calculations predict three major transitions in the low-energy region (Table S3). Excited state 5 is predicted at 721 nm and dominated (~63%) by $HOMO_{\alpha,\beta} \rightarrow LUMO_{\alpha,\beta}$ single-electron excitations. Since the HOMO/LUMO pairs with the same polarization (α- or β-set) have ~60/40% distribution on opposing phthalocyanine ligands, this excited state has a significant interligand charge-transfer (ILCT) character (i.e., Pc(1) → Pc(2) and Pc(2) → Pc(1) single-electron excitations). Thus, excited state 5 is responsible for the low-energy MCD B-term observed at 719 nm in the MCD spectrum of **1a**. On the other hand, predicted at 650 nm, excited states 9 and 10 form the classic pair of phthalocyanine-centered Q-bands that are dominated by the classic Gouterman's[85−87] $a_{1u} \rightarrow e_g$ (in the traditional D_{4h} symmetry notation) single-electron excitations localized on the same phthalocyanine ligands (i.e., Pc(1) → Pc(1) and Pc(2) → Pc(2) single-electron excitations). These two excited states are responsible for the MCD A-term, experimentally observed at 686 nm, in the MCD spectrum of **1a**. Thus, our TDDFT calculations for the first time, explained the experimentally observed MCD *B*- to A-term sequence (in ascending energy) in the low-energy region. The TDDFT-predicted energy of the Q-band in **1a** is also red-shifted compared to that predicted for **2Py**, which again agrees well with the experimental data. In the case of the triplet state of dimer **2Py**, TDDFT calculations predict a more

https://doi.org/10.1021/acs.inorgchem.3c00897
Inorg. Chem. 2023, 62, 10203−10220

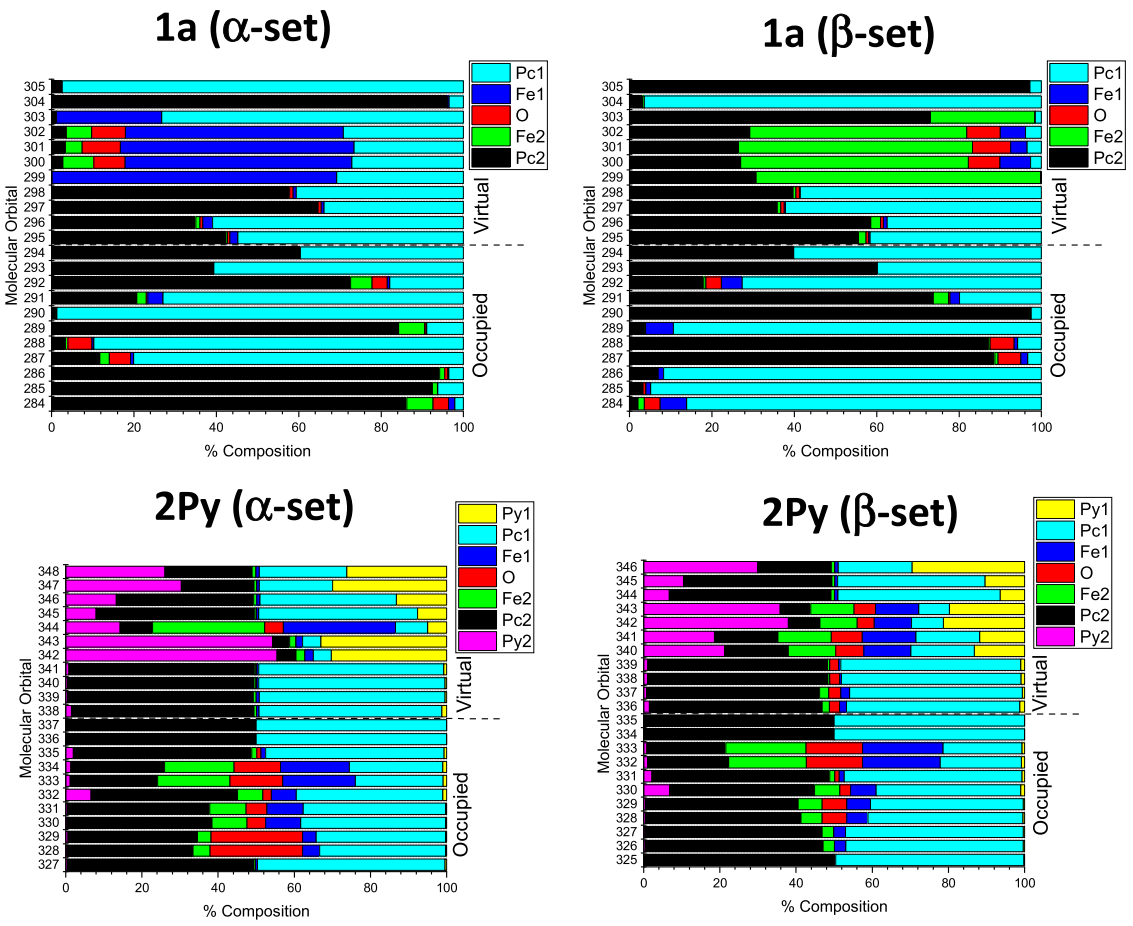

Figure 13. DFT-predicted compositions of frontier orbitals.

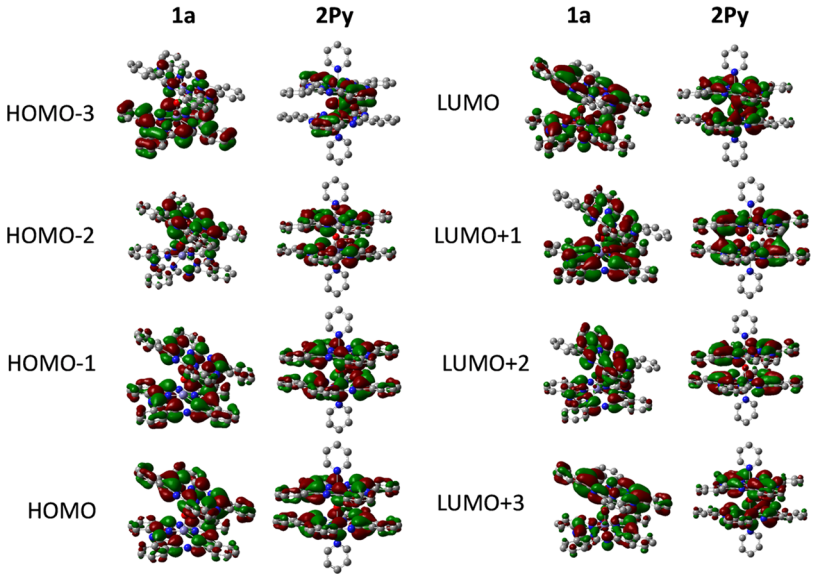

Figure 14. DFT-predicted images of select frontier orbitals (α-set; for full set of images, see the Supporting Information).

complex structure for the low-energy region of UV−vis and MCD spectra (Figure 15). However, the three most intense transitions again correlate well with the experimental data. In particular, excited state 15 ($f = 0.177$, 693 nm) has a significant charge-transfer (Fe(1,2)/O → Pc(1,2)) character and is dominated by HOMO − 3_β/HOMO − 2_β → LUMO + 5_β/LUMO + 4_β single-electron excitations. This excited state is responsible for the experimentally observed MCD B-term in this region. Excited states 20 and 22 ($f \sim 0.4$; 613 and 604 nm, respectively) belong to classic Gouterman's Q-band transitions that are dominated by the intraligand $a_{1u} \rightarrow e_g$ (in the traditional D_{4h} symmetry notation) single-electron excitations localized on the same phthalocyanine core. The TDDFT-predicted Q-band in **2Py** is shifted to a higher energy

https://doi.org/10.1021/acs.inorgchem.3c00897
Inorg. Chem. 2023, 62, 10203−10220

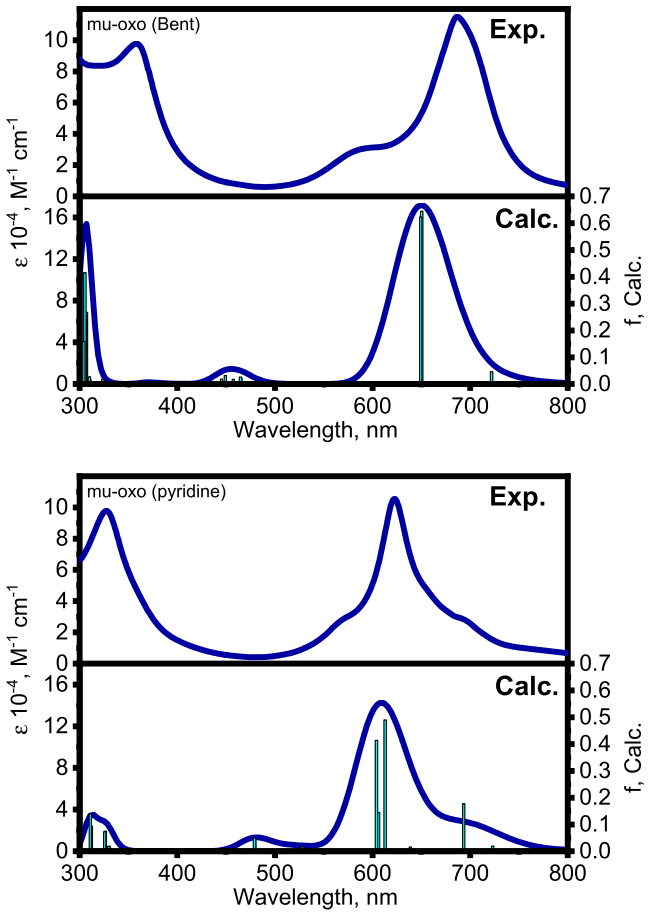

Figure 15. Experimental and TDDFT-predicted UV−vis spectra of **1a** (top) and **2Py** (bottom).

compared to those in **1a**, which agrees well with the experimentally observed blue shift in H-type phthalocyanine-based dimers. In agreement with the experimental data, TDDFT calculations predict the presence of the MCD B-term at lower energy than the Q-band centered MCD pseudo A-term in **2Py**. In agreement with the experimental data, the B-term/A-term energy splitting is larger in **2Py** (~2000 cm^{-1}) compared to the same energy splitting in **1a** (~1500 cm^{-1}). In theory, one might expect that the UV−vis and MCD spectra of bent **1a** and linear **1b** might be close to each other. Thus, we also conducted TDDFT calculations on the linear **1b** at the same level of theory. Indeed, TDDFT calculations predicted a degenerate Q-band in **1b** (651 nm; f = 0.66) close to that predicted in **1a** (650 nm; f = 0.63). However, in a higher-symmetry **1b** (D_4 point group), no nondegenerate transitions were predicted at the lower energy than the Q-band. Similar to Ishikawa's group calculations on Pc_2Sn and $[Pc_2Ln]^-$ systems, only one pair of degenerate excited states (705 nm; f = 0.0001) was predicted in this spectral envelope. This pair of transitions cannot explain the presence of an intense shoulder at 710 nm in a solution of dimer **1** and also cannot explain the presence of a strong MCD B-term associated with this experimental band as degenerate states in the diamagnetic phthalocyanine chromophore should lead to the observable A-term in the MCD spectrum of **1**.

DISCUSSION

The experimental data discussed above on μ-oxo complexes **1a**, **1b**, and **2Py** can be summarized as follows: (i) bent μ-oxo dimer **1a** is the only isomer present in solution, while both bent **1a** and linear **1b** can be isolated in the solid state; (ii) both **1a** and **1b** are diamagnetic compounds, which implies a strong antiferromagnetic coupling between their two high-spin iron(III) centers; (iii) the first and the second oxidation processes in **1a** are phthalocyanine-centered as confirmed by spectroelectrochemical data; (iv) **2Py** is a paramagnetic complex with two weakly antiferromagnetically coupled low-spin Fe(III) centers; (v) TDDFT calculations correctly predict a low-energy shift of the Q-band in **1a** compared to **2Py**. The remaining question is: What is the fundamental reason for the red-shifted Q-band in **1a** and blue-shifted Q-band in **2Py** when compared to the Q-band in monomeric PcFeX complexes? In the other words, why does **1a** behave as J-type, while **2Py** behaves as H-type aggregates? The Kasha classification[88] of H- and J-aggregates is solely based on the Coulombic intermolecular coupling and is successfully applied for the explanation of the aggregation processes in main-group and transition-metal phthalocyanines.[89] According to a simple

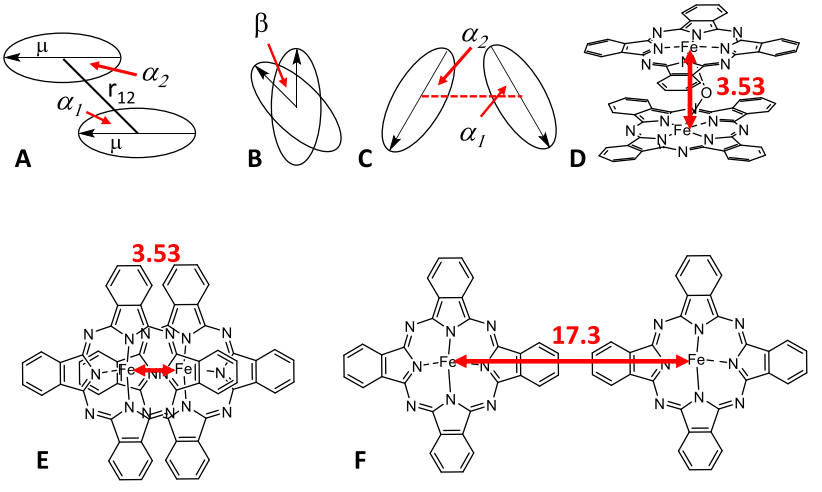

Figure 16. (A−C) Defined angles and distances for two dipole-coupled transitions as discussed in the text. (D) Fe−Fe (DFT) distance in **1a**. (E) Overlap between two phthalocyanine cores for r_{12} = 3.52 Å and $\alpha_1 = \alpha_2 = 0$. (F) r_{12} distance needed to avoid the overlap between two phthalocyanine cores for $\alpha_1 = \alpha_2 = 0$.

https://doi.org/10.1021/acs.inorgchem.3c00897
Inorg. Chem. 2023, 62, 10203−10220

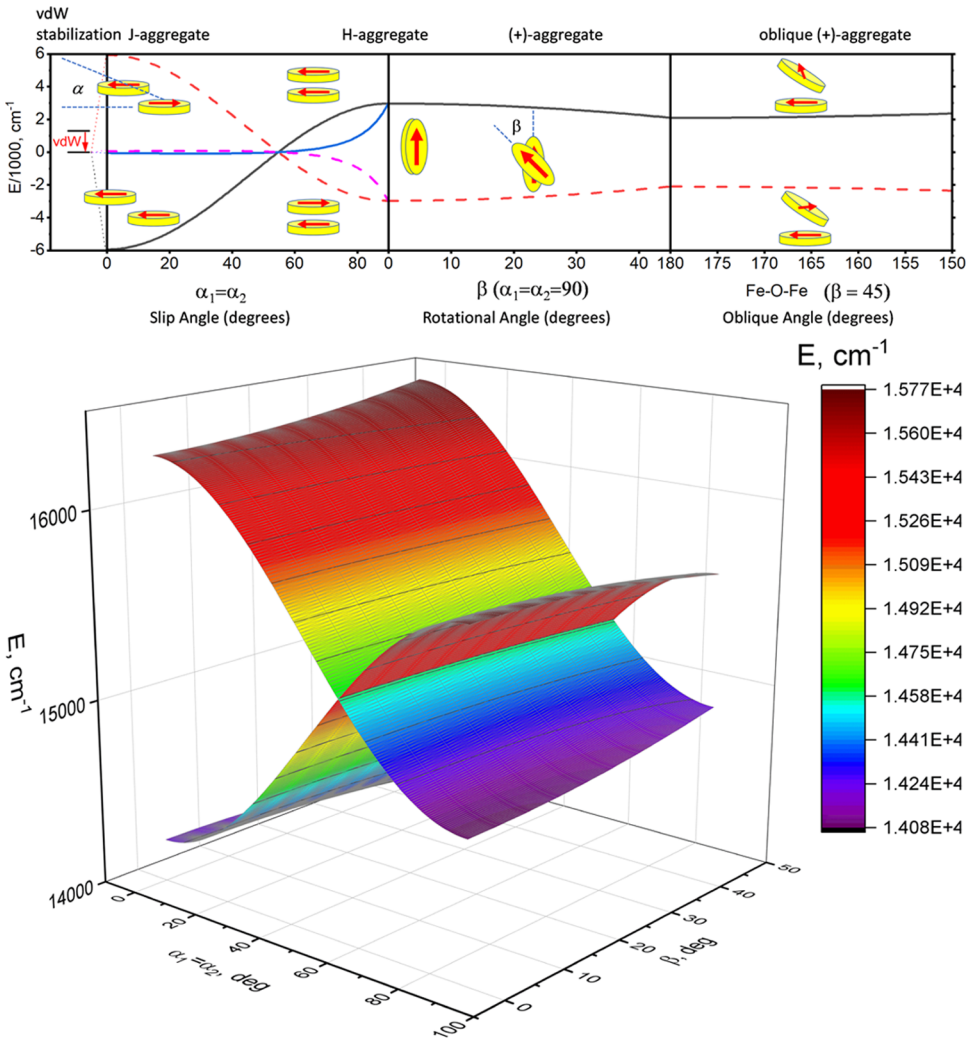

Figure 17. Top: two-dimensional (3D) profiles for the Coulomb coupling between two phthalocyanine chromophores as a function of slip angle α for two parallel macrocycles (left) positioned at a 3.53 Å Fe−Fe distance (black and red curves) or variable 3.53−17.3 Å Fe−Fe distance that avoids overlap between two macrocycles (blue and magenta curves, see Figure 16E,F for explanation); middle: Coulomb coupling as a function of β angle for two chromophores with $\alpha_1 = \alpha_2 = 90°$; right: Coulomb coupling for two chromophores as a function of the Fe−O−Fe angle. In all cases, the solid lines represent allowed and dashed lines represent forbidden transitions. Bottom: 3D plot for Coulomb coupling between two chromophores with 3.53 Å Fe−Fe distance and E_m = 15 250 cm^{-1} as a function of α and β angles.

exciton coupling theory, the Coulomb coupling between two phthalocyanine chromophores "1" and "2" can be predicted using eq 1a or 1b (below), with the angles and distances defined in Figure 16 ($E^{\pm}$ is the lower or upper energy band and E_m is the Q-band energy in the monomer)[88−90]

$$E^{\pm} = E_m \pm \frac{\mu^2(\sin(\alpha_1)\sin(\alpha_2)\cos(\beta) - 2\cos(\alpha_1)\cos(\alpha_2)}{r_{12}^3} \quad (1a)$$

$$E^{\pm} = E_m \pm \frac{\mu^2}{r_{12}^3}(\cos(\beta) - 3\cos(\alpha_1)\cos(\alpha_2)) \quad (1b)$$

Originally, Kasha[88] recognized two types of aggregation species (i.e., H- and J-aggregates) based on the relative orientation of the $S_0 \rightarrow S_1$ transition dipole moment (μ) and the angle (α, Figure 16A). In the case of J-aggregates, α is less than the "magic angle" of 54.7°, and the transition dipole moments maintain a "head-to-tail" orientation with a negative Coulomb coupling. The Coulomb coupling in the J-dimer results in the formation of two delocalized excited states that are split by 2|Jc| (Figure 17; note the initial stabilization offset caused by the van der Waals interaction energy). These two states are constructed by the in- and out-phase of two local excited states. The symmetric (in-phase) excited state has an enhanced transition dipole moment (with respect to the monomer) and is responsible for the red shift in the J-dimer, while the out-of-phase state is optically inactive (dark) because of the cancellation of the transition dipole moment.[88,89] In the case of the H-dimer, the in-phase state has a higher energy because of the positive Coulomb coupling, which results in a blue shift absorption band with respect to the monomer (Figure 17). When the transition dipole moments in two parallel chromophores are not aligned in a parallel or antiparallel manner, the additional angle β (Figure 16B) between the transition dipole moments should be taken into consideration using eq 1a or 1b. Taking into account the orthogonality of the doubly degenerate transition dipole moments in phthalocyanine molecules, the resulting splitting

https://doi.org/10.1021/acs.inorgchem.3c00897
Inorg. Chem. 2023, 62, 10203−10220

between 0 and 45° is shown in Figure 17. Finally, for the bent orientation of two chromophores, the angles are defined as shown in Figure 16C. The overall Coulombic profiles for selected cases are shown at the top of Figure 17, while the complete three-dimensional (3D) profile for such interactions is graphed on the bottom part of Figure 17.

The majority of phthalocyanine μ-oxo dimers possess a M−O−M angle[36,39] close to 180°,[91−95] which is also the geometry that was observed for the $[(1\text{-MeIm})PcFe]_2O$ complex reported by Ercolani and co-authors.[70] Thus, the use of a simple exciton coupling theory[88−90] described by eq 1a or 1b and shown in Figure 17 predicts the blue shift of the Q-band in paramagnetic $(PyPcFe)_2O$. The blue shift of the Q-band was also confirmed by the TDDFT calculations that predicted that the low-energy out-of-phase transitions are forbidden, and the in-phase transitions predicted at 613 and 604 nm are the only ones allowed. However, as discussed below, a simple exciton coupling theory cannot predict the presence of the bands observed at lower energy than the blue-shifted Q-band in this compound (Figure 15). Simple exciton coupling theory also failed to predict the red-shifted Q-band in $(PcFe)_2O$ and $(Pc^{tBu}Fe)_2O$ complexes at bent DFT-optimized geometry. Indeed, TDDFT calculations show that the Q-band observed in UV−vis and MCD spectra originates from the higher-energy in-phase doubly degenerate transition, so the bent μ-oxo dimer **1a** still should demonstrate H-aggregate behavior.

In order to explain the presence of both low- and high energy transitions (with respect to the Q-band energy in the monomeric analogues) in $[Pc_2Ln]^-$ and Pc_2Sn double-decker phthalocyanines, Ishikawa and co-workers developed an elegant model that takes into consideration charge-transfer (CT) transitions between two closely spaced cofacial phthalocyanine chromophores.[96−99] In the localized orbital basis, the interaction between local excitations within the individual Pc ligands "Pc_1" and "Pc_2" in the dimer generates two exciton-coupled (EC) excited states

$$|EC^{\pm}\rangle = \frac{\{|LE^{Pc1}\rangle \pm |LE^{Pc2}\rangle\}}{\sqrt{2}} \tag{2}$$

where LE represents the configurations expressing excitations localized on the individual phthalocyanine ligand. According to CI LCAO calculations conducted by Ishikawa and co-workers, the allowed EC^+ component should have a high intensity that is dominated by the expected configuration outlined in eq 3 (which quantifies the exciton coupling between two chromophores outlined in eq 1aa,b)

$$|6e_g \leftarrow 2a_{1u}EC^+\rangle = \frac{\{|6e_g^{Pc1} \leftarrow 2a_{1u}^{Pc1}\rangle + |6e_g^{Pc2} \leftarrow 2a_{1u}^{Pc2}\rangle\}}{\sqrt{2}} \tag{3}$$

Similarly, charge-transfer configurations in the cofacial phthalocyanine dimer give rise to two charge-resonance (CR) states

$$|CT^{\pm}\rangle = \frac{\{|CT^{Pc2\leftarrow Pc1}\rangle \pm |CT^{Pc1\leftarrow Pc2}\rangle\}}{\sqrt{2}} \tag{4}$$

where CT represents the charge-transfer configurations expressing excitations that involve electron transfer between two phthalocyanine ligands. According to CI LO calculations conducted by Ishikawa and co-workers, the allowed CR^+ component should have a lower intensity than the EC^+ excited state that is dominated by the expected configuration outlined in eq 5

$$|6e_g \leftarrow 2a_{1u}CT^+\rangle = \frac{\{|6e_g^{Pc2} \leftarrow 2a_{1u}^{Pc1}\rangle + |6e_g^{Pc1} \leftarrow 2a_{1u}^{Pc2}\rangle\}}{\sqrt{2}} \tag{5}$$

The energy of the allowed CR^+ state is higher than that of CT^+, and the energy difference between these two states decreases when the distance between two phthalocyanine ligands increases.

In the delocalized MO basis, the interaction between $HOMO_{Pc1,Pc2}$ and $LUMO_{Pc1,Pc2}$ results in the formation of four MOs

$$\varphi_1 = \frac{a-b}{\sqrt{2}}$$
$$\varphi_2 = \frac{a+b}{\sqrt{2}}$$
$$\varphi_1^* = \frac{j-k}{\sqrt{2}}$$
$$\varphi_2^* = \frac{j+k}{\sqrt{2}} \tag{6}$$

where a and b are the HOMO and j and k are the LUMO on Pc_1 and Pc_2, respectively. In this case, the single-electron excited states are

$$|^1(\varphi_2^* \leftarrow \varphi_1)\rangle = \frac{1}{\sqrt{2}}|EC^-\rangle + \frac{1}{\sqrt{2}}|CR^-\rangle$$
$$|^1(\varphi_1^* \leftarrow \varphi_1)\rangle = \frac{1}{\sqrt{2}}|EC^+\rangle - \frac{1}{\sqrt{2}}|CR^+\rangle$$
$$|^1(\varphi_2^* \leftarrow \varphi_2)\rangle = \frac{1}{\sqrt{2}}|EC^+\rangle + \frac{1}{\sqrt{2}}|CR^+\rangle$$
$$|^1(\varphi_1^* \leftarrow \varphi_2)\rangle = \frac{1}{\sqrt{2}}|EC^-\rangle - \frac{1}{\sqrt{2}}|CR^-\rangle \tag{7}$$

Both exciton and charge-transfer components are present in each of these wavefunctions and further configurational interactions should be considered for the final excited-state intensities. Both methods provide the same quantitative picture: (i) The two low-energy bands with the higher-energy component being more intense. (ii) The energy difference between two bands decreases with increasing interplanar Pc_1−Pc_2 distance. (iii) Both excited states are degenerate and should lead to two observable MCD A-terms in the low-energy region. The two predicted MCD A-terms were indeed observed in Pc_2Sn[96] and $[Pc_2Ln]^-$ (for the heavy Ln ions) complexes;[97−99] however, in the case of **1a** and **2Py**, no visible second low-energy MCD A-term was observed experimentally. This could be because of its low intensity (indeed, the TDDFT calculations indicated that this excited state should have an oscillator strength >0.001) or its closeness to the second higher-energy higher-intensity transition that is dominated by the EC^+ component in the LO basis. Indeed, no MCD A-term was observed in the red-tail region of the Q-band in the $[(RO)PcSi]_2O$ μ-oxo dimers with a Pc−Pc distance of ∼3.3 Å reported by Kobayashi and co-workers.[100] Moreover, Ishikawa's model does not explain the red-shifted Q-band in **1a** and the presence of the MCD B-terms in the low-energy regions of **1a** and **2Py**.

https://doi.org/10.1021/acs.inorgchem.3c00897
Inorg. Chem. 2023, 62, 10203−10220

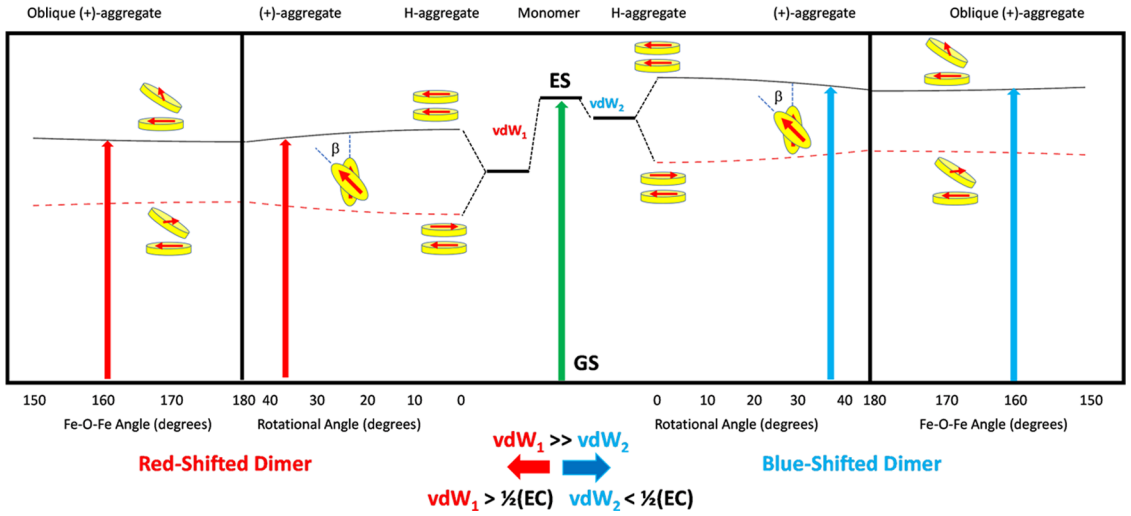

Figure 18. Formation of the red- and blue-shifted H-aggregates as a function of van der Waals stabilization energy. In both cases, Coulomb coupling is the same, but the van der Waals stabilization energy for the red-shifted H-aggregate is significantly larger than for the blue-shifted H-aggregate.

The red shift of the Q-band in $(PcFe)_2O$ and $(Pc^{tBu}Fe)_2O$ complexes can have two reasons. The simple reason is a larger stabilization of van der Waals energy between two phthalocyanine macrocycles in bent **1a** as compared to linear $(PyPc^{tBu}Fe)_2O$ (**2Py**, Figure 18). Indeed, the blue shift of the Q-band from the monomeric $Pc^{tBu}FeCl$ (**4Cl**) to $(PyPc^{tBu}Fe)_2O$ dimer **2Py** is ~935 cm^{-1} (~0.12 eV). Similarly, the red shift of the Q-band from the monomeric $Pc^{tBu}FeCl$ (**4Cl**) to bent $(Pc^{tBu}Fe)_2O$ dimer **1a** is only ~520 cm^{-1} (~0.06 eV). If one would assume that the van der Waals interaction between two phthalocyanine ligands in **1a** is ~3−5 kcal/mol stronger (1 kcal/mol is ~350 cm^{-1}) than the corresponding interaction in dimer **2Py**, then the red shift of the Q-band in **1a** would be possible to observe (Figure 18). In order to evaluate the van der Waals interaction energies in **1a** and **2Py**, we have replaced the Fe−O−Fe fragment in **1a** and **2Py** by four protons. In addition, the interaction energies for **2Py** were calculated in the presence and absence of the axial pyridine ligands. The overall trends predicted by DFT calculations seem to be independent of the basis set and exchange-correlation functional used (Table S4). The data clearly suggest that the energies of noncovalent interactions between two phthalocyanine macrocycles should be higher in the linear **2Py** than in the bent **1a**. Thus, the energy diagram shown in Figure 18 is highly likely incorrect and cannot be used for the explanation of the Q-band's red shift in **1a**.

An alternative explanation for the red-shifted Q-band in **1a** is the presence of additional transition(s) with lower than Q-band energies that cause the charge-transfer-induced perturbation of H-aggregate energies. The charge-transfer-induced H-aggregate behavior in perturbative and resonance regimes was described in detail by Spano's group.[101−106] Following Spano and co-workers, the energy shift of the allowed transition in J- and H-aggregates is reflective of the competition between the traditional Coulombic and CT-mediated intermolecular interactions that are simply quantified by J_C and J_{CT}, respectively (J_C is the Coulomb coupling and J_{CT} is the coupling caused by the CT). If $J_C + J_{CT} > 0$, then an H-type behavior will be observed for the dimer, while if $J_C + J_{CT} < 0$, J-type behavior is expected. Taking into consideration that signs of J_{CT} and J_C are independent from each other, one might expect that each dimer could fall under HH, HJ, JH, and JJ categories (with the first letter identifying J_{CT} and the second letter identifying J_C contributions).[101−106] Indeed, the red-shifted H-aggregates have been observed and explained using this model.

This qualitative framework discussed above is expected to be more complex for **1a** and **2Py** because of two additional items. First, while TDDFT calculations predict only one intense band with the Pc(1)/Pc(2) → Pc(2)/Pc(1) CT character between out-of-phase and in-phase Q-band transitions for bent **1a**, three bands with significant intensities and CT character were predicted for **2Py** in the same spectral region. Thus, in the latter case, it is logical to use ΣJ_{CT} instead of J_{CT}. The second complication comes from the presence of an additional Fe−O−Fe superexchange coupling pathway. To the best of our knowledge, the contribution of such coupling to the overall behavior of H- and J-aggregates has yet to be considered or quantified. Based on the magnetic susceptibility data, the antiferromagnetic coupling constants for bent **1a** and linear **2Py** differ dramatically (a large coupling constant is required for the diamagnetic ground state in **1a**, while a small coupling constant was observed for paramagnetic **2Py**) and thus, we can expect that the magnitude of J_{SE} (J_{SE} is a superexchange-mediated coupling) would also be very different for these complexes. When such coupling is considered, one might expect that the overall H-type and J-type behavior will reflect a $J_C + \Sigma J_{CT} + J_{SE} > 0$ or $J_C + \Sigma J_{CT} + J_{SE} < 0$ balance, respectively, where the sign of each term is independent from the other two terms.

From our simple geometric and DFT considerations on **1a** and **2Py**, we are confident that the value of J_C for both dimers is positive (the blue shift of the Q-band is expected). The Q-band position of the allowed in-phase transition in **2Py** (627 nm) is very close to that observed for linear $[(R_1O)Pc^{R2n}Si]_2O$ and $(PcAl)_2O$ μ-oxo dimers, which, in a crude approximation, meaning that the contribution from the ΣJ_{CT} and J_{SE} terms in this compound is rather small. In this case, the J_C-term dominates and the observed blue shift of the Q-band can be described by classic Kasha's theory.[88] This is apparently not the case for bent **1a**. In order to have a $J_C + \Sigma J_{CT} + J_{SE} < 0$ relationship and thus red-shifted Q-band, the negative (ΣJ_{CT} +

https://doi.org/10.1021/acs.inorgchem.3c00897
Inorg. Chem. 2023, 62, 10203−10220

J_{SE}) contribution should be on the order of 2000 cm^{-1}. Both terms for **1a** should be very different from those for **2Py** and thus one should not be surprised by the different magnitude of the ΣJ_{CT} and J_{SE} terms. Currently, there is no simple way to estimate these terms computationally. However, TDDFT calculations take into consideration all $\pi-\pi^*$ and CT transitions by definition and as discussed above, support our point of view. Indeed, TDDFT correctly predicts a blue shift for complex **2Py** and a red shift for complex **1a**. TDDFT also correctly predicted a nondegenerate CT excited state at lower than Q-band energy in **1a** that correlates with the UV−vis and MCD data on this compound. Finally, TDDFT correctly predicted several CT transitions for **2Py** with energies lower than the *Q*-band.

CONCLUSIONS

Similar to previous reports, Mössbauer spectra of solid-state samples of the $(Pc^{tBu}Fe)_2O$ complex consist of two doublets that represent diamagnetic bent **1a** and linear **1b** isomers. The ratio between two isomers depends on the purification method. Once frozen in a non-coordinating solvent, the Mössbauer spectrum consists of **1a**, but not **1b**, which explains the identical UV−vis and MCD spectra of **1** once dissolved in the non-coordinating solvent. The UV−vis and MCD spectra of **1a** have a negligible temperature dependence. The MCD spectrum of **1a** has one Faraday A- and one B-term between 670 and 720 nm, which correlate with the 690 nm band and 709 nm shoulder observed in the respective UV−vis spectra of this compound. Up to three oxidation and four reduction processes were observed within the CV and DPV of **1a**. Oxidation of **1a** in non-coordinating solvents gives rise to broad NIR bands around 1195 nm (first oxidation) and 1264 nm (second oxidation). A Faraday B-term with negative amplitude was observed in the NIR region. The UV−vis and MCD spectra of $[\mathbf{1a}]^+$ and $[\mathbf{1a}]^{2+}$ are very different from those in monomeric $Pc^{tBu}(1-)Fe^{III}X_2$ complexes **5X** (X = Cl^- or $CF_3CO_2^-$). **2Py** is paramagnetic (μ_B = 2.19, g = 2.11, and J = −6.1 cm^{-1}) and has a major peak at 627 nm in its UV−vis spectrum, which is associated with an MCD pseudo A-term. DFT and TDDFT calculations were used to explain the unusually red-shifted *Q*-band region in **1a** as well as the H-aggregate-like spectra of **2Py**. Analysis of the spectra of **1a** and **2Py** using Kasha's and Spano's exciton coupling theories is suggestive of the mixing of low-energy $\pi-\pi^*$ and CT transitions in the low-energy region.

EXPERIMENTAL SECTION

Materials. All solvents were purchased from commercial sources and purified using standard procedures. All phthalocyanine-based compounds described herein were prepared as described previously.[45,61] We found that the **1a**/**1b** ratio depends on the reaction solvent used. In the case when the metalation reaction was conducted in *N*,*N*-dimethylaminoethanol and the reaction mixture was precipitated by adding water prior column chromatography on basic Al_2O_3 (using toluene−hexane as eluent), the **1b** isomer would dominate as the reaction product (as determined by Mössbauer spectroscopy; see Figure 2). However, when complex **1** was prepared without a solvent or in a nonpolar aromatic high boiling point solvent (*o*-dichlorobenzene or 1-chloronaphthalene) and directly loaded on column with basic Al_2O_3, **1a** isomer would dominate as the reaction product (as determined by Mössbauer spectroscopy; see Figure S1).

Mössbauer Spectroscopy. ^{57}Fe Mössbauer spectra were collected either at 10 K or room temperature. ^{57}Fe Mössbauer spectroscopy experiments were performed in zero field in a transmission geometry with a 10 GBq ^{57}Co-in-Rh source and either WissEl or NGRS-4 constant acceleration drive. All spectra were calibrated relative to α-Fe or sodium nitroprusside at room temperature. A nonlinear least squares analysis was applied to ^{57}Fe Mössbauer spectra for fitting. Each Fe-site was characterized by a Lorentzian lineshape doublet and an isomer shift whose energies were set by the appropriate nuclear transitions. In-house-produced codes or Mossfit software were used for the data analyses. Relative uncertainties for the fitted spectra are ΔIS = 2% and ΔQS = 1% for all samples.

Magnetism. Magnetometry experiments were performed on samples using a Quantum Design Magnetic Properties Measurement System (MPMS XL-5). Instrument calibration was performed using a Pd standard (National Bureau of Standards Reference Material 765). Samples were mounted in sealed NMR tubes, and the solvent's susceptibility was subtracted from the data presented. Measurements were performed in a 1 T field.

In the case of the binuclear molecule with two interacting paramagnetic centers, the general isotropic exchange Hamiltonian has one exchange and two values

$$\hat{H} = -2JS_1S_2 \tag{8}$$

The solution for $S_1 = S_2 = 1/2$ basis set (e.g., **2Py**) using Hamiltonian (eq 8) leads to the Bleaney−Bowers equation for magnetic susceptibility (eq 9)[107]

$$\chi = \frac{Ng^2\mu_B^2}{kT}\frac{2\,e^{2x}}{1+3\,e^{2x}} \tag{9}$$

where $\chi = J/kT$.

Electrochemical Measurements. The electrochemical data were collected using a CH-620 analyzer with platinum working, platinum auxiliary, and Ag/AgCl pseudo-reference electrodes. Ferrocene was used as an internal standard for the studied compounds and the reported potentials were corrected to the FcH/FcH^+ couple. These potentials then were corrected to SCE. All electrochemical experiments were conducted using either a DCM/0.1 M tetrabutylammonium perchlorate (TBAP) or DCM/0.05 M tetrabutylammonium tetrakis(pentafluorophenyl)borate (TFAB) system.

Spectroelectrochemical Measurements. Spectroelectrochemical experiments were performed using a Jasco V-770 UV−vis−NIR spectrophotometer in tandem with a CH Instruments CH-620 electrochemical analyzer that was operated using the bulk electrolysis mode. The data were collected using a custom-made 1 mm cell, a platinum mesh working electrode, platinum auxiliary electrode, Ag/AgCl pseudo-reference electrode, and either a DCM/0.3 M TBAP or DCM/0.15 M TBAF system.

Computational Aspects. All calculations were run using Gaussian 16.[108] HISSbPBE[109] with Wachter's full-electron basis set[110] (Wf) for iron and the 6-311G(d) basis set[111] for the other atoms were used for all geometry optimizations. Vibrational frequencies were calculated to ensure all geometries were local minima. Time-dependent density functional theory (TDDFT) with BP86,[112,113] BP86-D3,[112−114] BP86-D3BJ,[112−115] tHCTHhyb,[116] B97,[117] B97-D3,[114,117] B3LYP,[118] B3LYP-D3,[114,118] B3LYP-D3BJ,[114,115,118] X3LYP,[119] APDF,[120] PBE0,[121] SHEPBE,[122] OHS2PBE,[123] PBEhPBE,[121] B98,[124] B97-1,[125] B97-2,[126] M06,[127] M06-D3,[114,127] M05,[128] N12,[129] MN12SX,[130] MN12L,[131] wB97,[132] wB97x,[133] CAM-B3LYP,[133] wB97XD,[134] SOGGA11X,[135] and HISSbPBE[109] was tested on for the compound reported herein. Single-point calculations using the same parameters as the TDDFT calculations were also performed. All calculations were run in solution using the PCM model,[136] with dichloromethane (DCM) as the solvent. In each case, the peripheral *t*Bu groups were shortened to methyls to minimize computational cost. QMForge[137] was used for the molecular orbital composition analyses.

We used Yamaguchi's formula[138] for the evaluation of coupling constant J in **1a** and **2Py** as it covers both weak and strong coupling limit and was successfully applied in the modeling of a large array of dinuclear complexes using DFT methods[139]

https://doi.org/10.1021/acs.inorgchem.3c00897
Inorg. Chem. 2023, 62, 10203−10220

$$J = -\frac{E_{HS} - E_{BS}}{\langle \hat{S}^2 \rangle_{HS} - \langle \hat{S}^2 \rangle_{BS}}$$

where E_{HS} and E_{BS} are DFT energies of the high-spin and broken-symmetry calculations and $\langle \hat{S}^2 \rangle$ values are the total spin angular momenta expectation values for Kohn–Sham determinants.

UV–Vis and MCD Spectroscopy. All UV–vis spectra were collected on a Jasco V-770 spectrophotometer and MCD spectra were measured with a Jasco J-1500 CD spectrometer using a Jasco MCD-581 electromagnet operated at 1.0 T or permanent magnet operated at 1.6 T. The completed MCD spectra were measured at 10 °C in parallel and antiparallel orientations with respect to the magnetic field. The MCD spectra were recorded in terms of mDeg = $[\theta]$ on the y-axis and were converted to molar ellipticity via $\Delta\varepsilon = \theta/(32\,980Blc)$, where B is the magnetic field, l is the path length (cm), and c is the concentration (M).[140] For detailed explanation of the Faraday A-, B-, and C-terms, including pseudo A-terms when applied to porphyrinoids including phthalocyanines, readers can refer to excellent reviews published by Stillman and co-workers.[140,141]

■ ASSOCIATED CONTENT

Supporting Information

The Supporting Information is available free of charge at https://pubs.acs.org/doi/10.1021/acs.inorgchem.3c00897.

Additional experimental and computational data (PDF)

■ AUTHOR INFORMATION

Corresponding Authors

Victor N. Nemykin − *Department of Chemistry, University of Tennessee, Knoxville, Tennessee 37916, United States; Department of Chemistry, University of Manitoba, Winnipeg, Manitoba R3T 2N2, Canada; Department of Chemistry & Biochemistry, University of Minnesota, Duluth, Duluth, Minnesota 55812, United States;* orcid.org/0000-0003-4345-0848; Email: vnemykin@utk.edu

Johan van Lierop − *Department of Physics & Astronomy, University of Manitoba, Winnipeg, Manitoba R3T 2N2, Canada*; Email: johan@physics.umanitoba.ca

Authors

Briana R. Schrage − *Department of Chemistry, University of Tennessee, Knoxville, Tennessee 37916, United States*

Dustin E. Nevonen − *Department of Chemistry, University of Tennessee, Knoxville, Tennessee 37916, United States; Department of Chemistry, University of Manitoba, Winnipeg, Manitoba R3T 2N2, Canada*

Laurel A. Harrison − *Department of Chemistry, University of Tennessee, Knoxville, Tennessee 37916, United States*

Kelly M. E. Newman − *Department of Physics & Astronomy, University of Manitoba, Winnipeg, Manitoba R3T 2N2, Canada*

Vinod K. Paidi − *Department of Physics & Astronomy, University of Manitoba, Winnipeg, Manitoba R3T 2N2, Canada*

Complete contact information is available at: https://pubs.acs.org/10.1021/acs.inorgchem.3c00897

Notes

The authors declare no competing financial interest.

■ ACKNOWLEDGMENTS

The generous computing time offered by the University of Minnesota Supercomputing Institute to V.N.N. is greatly appreciated (CHE-2153081). This work was partially supported by the University of Minnesota Grant-in-Aid. The authors acknowledge Prof. Nagao Kobayashi for providing the opportunity to record the MCD spectrum of **1a** at low temperature, and Prof. Claudio Ercolani for the stimulating discussion. The authors thank Dr. Konstantinos D. Vogiatzis and Brett A. Smith for fruitful discussions on the computational aspects of this project. J.v.L. acknowledges funding from the Natural Sciences and Engineering Research Council of Canada (RGPIN-2018-05012) and the Canada Foundation for Innovation.

■ REFERENCES

(1) Nemykin, V. N.; Tret'yakova, I. N.; Volkov, S. V.; Li, V. D.; Mekhryakova, N. G.; Kaliya, O. L.; Luk'yanets, E. A. Synthesis, structure and properties of coordination compounds of iron phthalocyanines and their analogues. *Russ. Chem. Rev.* **2000**, *69*, 325–346.

(2) Hanack, M. In *Phthalocyanines: Properties and Applications*; Leznoff, C. C.; Lever, A. B. P., Eds.; VCH: New York, 1989; Vol. 2, pp 43–96.

(3) Ercolani, C.; Floris, B. In *Phthalocyanines: Properties and Applications*; Leznoff, C. C.; Lever, A. B. P., Eds.; VCH: New York, 1989; Vol. 2, pp 1–43.

(4) Taube, R. New aspects of the chemistry of transition metal phthalocyanines. *Pure Appl. Chem.* **1974**, *38*, 427–438.

(5) Sorokin, A. B. Phthalocyanine Metal Complexes in Catalysis. *Chem. Rev.* **2013**, *113*, 8152–8191.

(6) Kennedy, B. J.; Murray, K. S.; Zwack, P. R.; Homborg, H.; Kalz, W. Spin states in iron(III) phthalocyanines studied by Moessbauer, magnetic susceptibility, and ESR measurements. *Inorg. Chem.* **1986**, *25*, 2539–2545.

(7) L'Her, M.; Pondave, A. In *The Porphyrin Handbook*; Kadish, K. M.; Smith, K.; Guilard, R., Eds.; Academic Press, 2003; Vol. *16*, pp 117–170.

(8) Sternberg, E. D.; Dolphin, D.; Bruckner, C. Porphyrin-based photosensitizers for use in photodynamic therapy. *Tetrahedron* **1998**, *54*, 4151–4202.

(9) Jasat, A.; Dolphin, D. Expanded Porphyrins and Their Heterologs. *Chem. Rev.* **1997**, *97*, 2267–2340.

(10) Kim, J.; Oh, J.; Osuka, A.; Kim, D. Porphyrinoids, a unique platform for exploring excited-state aromaticity. *Chem. Soc. Rev.* **2022**, *51*, 268–292.

(11) Lavarda, G.; Labella, J.; Martinez-Diaz, M. V.; Rodriguez-Morgade, M. S.; Osuka, A.; Torres, T. Recent advances in subphthalocyanines and related subporphyrinoids. *Chem. Soc. Rev.* **2022**, *51*, 9482–9619.

(12) Wang, K.; Osuka, A.; Song, J. Pd-Catalyzed Cross Coupling Strategy for Functional Porphyrin Arrays. *ACS Cent. Sci.* **2020**, *6*, 2159–2178.

(13) Arambula, J. F.; Sessler, J. L. Porphyrinoid Drug Conjugates. *Chem* **2020**, *6*, 1634–1651.

(14) Fukuzumi, S.; Lee, Y.-M.; Nam, W. Photocatalytic redox reactions with metalloporphyrins. *J. Porphyrins Phthalocyanines* **2020**, *24*, 21–32.

(15) Brewster, J. T., II; Zafar, H.; Root, H. D.; Thiabaud, G. D.; Sessler, J. L. Porphyrinoid f-Element Complexes. *Inorg. Chem.* **2020**, *59*, 32–47.

(16) Gomes, A. T. P. C.; Neves, M. G. P. M. S.; Cavaleiro, J. A. S. Cancer, photodynamic therapy and porphyrin-type derivatives. *An. Acad. Bras. Cienc.* **2018**, *90*, 993–1026.

(17) Fukuzumi, S.; Nam, W. Thermal and photoinduced electron-transfer catalysis of high-valent metal-oxo porphyrins in oxidation of substrates. *J. Porphyrins Phthalocyanines* **2016**, *20*, 35–44.

(18) Bill, N. L.; Trukhina, O.; Sessler, J. L.; Torres, T. Supramolecular electron transfer-based switching involving pyrrolic macrocycles. A new approach to sensor development? *Chem. Commun.* **2015**, *51*, 7781–7794.

(19) Orman, E. B.; Yazar, Z.; Piskin, M.; Odabas, Z.; Ozkaya, A. R. Novel 2,6-dimethoxyphenoxy alpha substituted phthalocyaninato metal complexes: Electrochemistry, In situ spectroelectrochemistry and oxygen electrocatalysis. *Synth. Met.* **2022**, *290*, No. 117139.
(20) Zhang, W.; Meeus, E. J.; Wang, L.; Zhang, L.-H.; Yang, S.; de Bruin, B.; Reek, J. N. H.; Yu, F. Boosting Electrochemical Oxygen Reduction Performance of Iron Phthalocyanine through Axial Coordination Sphere Interaction. *ChemSusChem* **2022**, *15*, No. e202102379.
(21) Qian, J.; Liu, Y.; Zheng, W.; Zhou, B.; Dong, X. Covalent Modification of Iron Phthalocyanine into Skeleton of Graphitic Carbon Nitride and Its Visible-Light-Driven Photocatalytic Reduction of Nitroaromatic Compounds. *Catalysts* **2022**, *12*, No. 752.
(22) Mukherjee, B. Solvothermally Synthesized Iron Phthalocyanine Nanostructure for High ORR Response: A Joint Experimental Investigation and DFT Analysis. *J. Electrochem. Soc.* **2020**, *167*, No. 116501.
(23) Sun, C.; Li, Z.; Yang, J.; Wang, S.; Zhong, X.; Wang, L. Two-dimensional closely packed amide polyphthalocyanine iron absorbed on Vulcan XC-72 as an efficient electrocatalyst for oxygen reduction reaction. *Catal. Today* **2020**, *353*, 279−286.
(24) Neamtu, M.; Nadejde, C.; Brinza, L.; Dragos, O.; Gherghel, D.; Paul, A. Iron phthalocyanine-sensitized magnetic catalysts for BPA photodegradation. *Sci. Rep.* **2020**, *10*, No. 5376.
(25) Herrera, S.; Tasca, F.; Williams, F. J.; Calvo, E. J. Adsorption of 4,4′-Dithiodipyridine Axially Coordinated to Iron(II) Phthalocyanine on Au(111) as a New Strategy for Oxygen Reduction Electrocatalysis. *ChemPhysChem* **2018**, *19*, 1599−1604.
(26) Mihara, N.; Yamada, Y.; Takaya, H.; Kitagawa, Y.; Aoyama, S.; Igawa, K.; Tomooka, K.; Tanaka, K. Oxygen Reduction to Water by a Cofacial Dimer of Iron(III)-Porphyrin and Iron(III)-Phthalocyanine Linked through a Highly Flexible Fourfold Rotaxane. *Chem.—Eur. J.* **2017**, *23*, 7508−7514.
(27) Neu, H. M.; Zhdankin, V. V.; Nemykin, V. N. Binuclear iron(III) phthalocyanine(μ-oxodimer)/tetrabutylammonium oxone: a powerful catalytic system for oxidation of hydrocarbons in organic solution. *Tetrahedron Lett.* **2010**, *51*, 6545−6548.
(28) Neu, H. M.; Yusubov, M. S.; Zhdankin, V. V.; Nemykin, V. N. Binuclear iron(III) phthalocyanine(μ-oxo-dimer)-catalyzed oxygenation of aromatic hydrocarbons with iodosylbenzene sulfate and iodosylbenzene as the oxidants. *Adv. Synth. Catal.* **2009**, *351*, 3168−3174.
(29) Geraskin, I. M.; Luedtke, M. W.; Neu, H. M.; Nemykin, V. N.; Zhdankin, V. V. Organic iodine(V) compounds as terminal oxidants in iron(III) phthalocyanine catalyzed oxidation of alcohols. *Tetrahedron Lett.* **2008**, *49*, 7410−7412.
(30) Yusubov, M. S.; Celik, C.; Geraskina, M. R.; Yoshimura, A.; Zhdankin, V. V.; Nemykin, V. N. Binuclear iron(III) octakis-(perfluorophenyl)tetraazaporphyrin μ-oxodimer: a highly efficient catalyst for biomimetic oxygenation reactions. *Tetrahedron Lett.* **2014**, *55*, 5687−5690.
(31) Sorokin, A. B.Cleavage of C-F Bonds in Oxidative Conditions Mediated by Transition Metal Complexes. *Advances in Inorganic Chemistry*; Elsevier Inc., 2022; Vol. *79*, pp 23−63.
(32) Sorokin, A. B. From mononuclear iron phthalocyanines in catalysis to micro-nitrido diiron complexes and beyond. *Catal. Today* **2021**, *373*, 38−58.
(33) Cailler, L. P.; Clemancey, M.; Barilone, J.; Maldivi, P.; Latour, J.-M.; Sorokin, A. B. Comparative Study of the Electronic Structures of μ-Oxo, μ-Nitrido, and μ-Carbido Diiron Octapropylporphyrazine Complexes and Their Catalytic Activity in Cyclopropanation of Olefins. *Inorg. Chem.* **2020**, *59*, 1104−1116.
(34) Sorokin, A. B. Recent progress on exploring μ-oxo bridged binuclear porphyrinoid complexes in catalysis and material science. *Coord. Chem. Rev.* **2019**, *389*, 141−160.
(35) Colomban, C.; Tobing, A. H.; Mukherjee, G.; Sastri, C. V.; Sorokin, A. B.; de Visser, S. P. Mechanism of Oxidative Activation of Fluorinated Aromatic Compounds by N-Bridged Diiron-Phthalocyanine: What Determines the Reactivity? *Chem.—Eur. J.* **2019**, *25*, 14320−14331.
(36) Afanasiev, P.; Sorokin, A. B. μ-Nitrido Diiron Macrocyclic Platform: Particular Structure for Particular Catalysis. *Acc. Chem. Res.* **2016**, *49*, 583−593.
(37) Quesne, M. G.; Senthilnathan, D.; Singh, D.; Kumar, D.; Maldivi, P.; Sorokin, A. B.; de Visser, S. P. Origin of the Enhanced Reactivity of μ-Nitrido-Bridged Diiron(IV)-Oxo Porphyrinoid Complexes over Cytochrome P450 Compound I. *ACS Catal.* **2016**, *6*, 2230−2243.
(38) Colomban, C.; Kudrik, E. V.; Tyurin, D. V.; Albrieux, F.; Nefedov, S. E.; Afanasiev, P.; Sorokin, A. B. Synthesis and characterization of μ-nitrido, μ-carbido and μ-oxo dimers of iron octapropylporphyrazine. *Dalton Trans.* **2015**, *44*, 2240−2251.
(39) Colomban, C.; Kudrik, E. V.; Briois, V.; Shwarbrick, J. C.; Sorokin, A. B.; Afanasiev, P. X-ray Absorption and Emission Spectroscopies of X-Bridged Diiron Phthalocyanine Complexes (FePc)2X (X = C, N, O) Combined with DFT Study of (FePc)2X and Their High-Valent Diiron Oxo Complexes. *Inorg. Chem.* **2014**, *53*, 11517−11530.
(40) Sorokin, A. B.; Kudrik, E. V.; Bouchu, D. Bio-inspired oxidation of methane in water catalyzed by N-bridged diiron phthalocyanine complex. *Chem. Commun.* **2008**, 2562−2564.
(41) Kudrik, E. V.; Afanasiev, P.; Bouchu, D.; Millet, J.-M. M.; Sorokin, A. B. Diiron N-bridged species bearing phthalocyanine ligand catalyzes oxidation of methane, propane and benzene under mild conditions. *J. Porphyrins Phthalocyanines* **2008**, *12*, 1078−1089.
(42) Choi, H. J.; Kwag, G.; Kim, S. Electrochemical and XAFS investigation of nitrite reduction by heat-treated μ-oxo derivative of iron phthalocyanine supported on high area carbon. *J. Electroanal. Chem.* **2001**, *508*, 105−114.
(43) Chen, M. J.; Fremgen, D. E.; Rathke, J. W. Oxygen atom transfer from μ-Oxobis[1,4,8,11,15,18,22,25-octakis(trifluoromethyl)-phthalocyaninato]diiron(III): Evidence for an FeIV=O intermediate. *J. Porphyrins Phthalocyanines* **1998**, *2*, 473−482.
(44) Ravikanth, M.; Achim, C.; Tyhonas, J. S.; Munck, E.; Lindsey, J. S. Investigation of phthalocyanine catalysts for the aerobic synthesis of meso-substituted porphyrins. *J. Porphyrins Phthalocyanines* **1997**, *1*, 385−394.
(45) Sievertsen, S.; Murray, K. S.; Moubaraki, B.; Berry, K. J.; Korbatieh, Y.; Cashion, J. D.; Brown, L. J.; Homborg, H. Dimeric low-spin iron(III) phthalocyanines: synthesis and properties of ferromagnetically coupled μ-oxodi(acidophthalocyaninatoferrates(III). *Z. Anorg. Allg. Chem.* **1994**, *620*, 1203−1212.
(46) Bakshi, E. N.; Murray, K. S. Applied field Moessbauer spectra of low-spin mononuclear and binuclear iron(III)-phthalocyanines. *Hyperfine Interact.* **1988**, *40*, 283−286.
(47) Kennedy, B. J.; Murray, K. S.; Zwack, P. R.; Homborg, H.; Kalz, W. μ-Oxo iron(III) phthalocyanine. Electronic structure of the solid form obtained from a dihydroxoiron(III) precursor. *Inorg. Chem.* **1985**, *24*, 3302−3305.
(48) Frampton, C. S.; Silver, J. A Moessbauer investigation of the interaction of (phthalocyaninato)iron(II) with molecular oxygen. Evidence for only one form of (μ-oxo)bis(phthalocyaninato)iron(III) is found. *Inorg. Chim. Acta* **1985**, *96*, 187−191.
(49) Ercolani, C.; Gardini, M.; Monacelli, F.; Pennesi, G.; Rossi, G. Interaction of (phthalocyaninato)iron(II) with molecular oxygen: synthesis and characterization of two different crystalline forms of (μ-oxo)bis[(phthalocyaninato)iron(III)]. *Inorg. Chem.* **1983**, *22*, 2584−2589.
(50) Ercolani, C.; Gardini, M.; Pennesi, G.; Rosse, G. Oxygen atom transfer in the oxidation of triphenylphosphine by μ-oxo-bis-[phthalocyaninatoiron(III)]. *J. Chem. Soc., Chem. Commun.* **1983**, 549−550.
(51) Ercolani, C.; Rossi, G.; Monacelli, F. Synthesis and characterization of a μ-oxo dimer formed by the interaction of phthalocyanine iron(II) with dioxygen. *Inorg. Chim. Acta* **1980**, *44*, L215−L216.

https://doi.org/10.1021/acs.inorgchem.3c00897
Inorg. Chem. 2023, 62, 10203−10220

(52) Ercolani, C.; Floris, B. In *Phthalocyanines: Properties and Applications*; Leznoff, C. C.; Lever, A. B. P., Eds.; VCH Publishers: New York, 1993; Vol. 2, pp 1−42.
(53) Ercolani, C.; Floris, B. In *Phthalocyanines: Properties and Applications*; Leznoff, C. C.; Lever, A. B. P., Eds.; VCH Publishers: New York, 1996; Vol. 4, pp 405−426.
(54) Dieing, R.; Schmid, G.; Witke, E.; Feucht, C.; Dressen, M.; Pohmer, J.; Hanack, M. Soluble substituted μ-oxo(phthalocyaninato)-iron(III) dimers. *Chem. Ber.* **1995**, *128*, 589−598.
(55) Nemykin, V. N.; Chernii, V. Y.; Volkov, S. V.; Bundina, N. I.; Kaliya, O. L.; Li, V. D.; Lukyanets, E. A. Further studies on the oxidation state of iron in μ-oxo dimeric phthalocyanine complexes. *J. Porphyrins Phthalocyanines* **1999**, *3*, 87−98.
(56) Ercolani, C.; Gardini, M.; Murray, K. S.; Pennesi, G.; Rossi, G. Crystalline isomerism in (μ-oxo)bis[(phthalocyaninato)iron(III)]: Further characterization of the isomer having a linear or quasi-linear Fe-O-Fe bond system (μ-oxo(2). *Inorg. Chem.* **1986**, *25*, 3972−3976.
(57) Ercolani, C.; Gardini, M.; Murray, K. S.; Pennesi, G.; Rossi, G.; Zwack, P. R. Molecular and electronic structure of six-coordinate low-spin oxo-bridged dimers formed by the interaction of (μ-oxo)bis-((phthalocyaninato)iron(III)) with nitrogen bases. *Inorg. Chem.* **1987**, *26*, 3539−3543.
(58) Myers, J. F.; Canham, G. W. R.; Lever, A. B. P. Higher oxidation level phthalocyanine complexes of chromium, iron, cobalt and zinc. Phthalocyanine radical species. *Inorg. Chem.* **1975**, *14*, 461−468.
(59) Canham, G. W. R.; Myers, J.; Lever, A. B. P. Higher oxidation state iron and cobalt phthalocyanine derivatives. Phthalocyanine radical cation complexes. *J. Chem. Soc., Chem. Commun.* **1973**, 483−484.
(60) Silver, J.; Lukes, P.; Houlton, A.; Howe, S.; Hey, P.; Ahmet, M. T. Electrochromism in the transition-metal phthalocyanines. Part 3. Molecular organization, reorganization and assembly under the influence of an applied electric field. Response of [Fe(pc)] and [Fe(pc)Cl]. *J. Mater. Chem.* **1992**, *2*, 849−855.
(61) Nevonen, D. E.; Rohde, G. T.; Nemykin, V. N. New Insight Into an Old Problem: Analysis, Interpretation, and Theoretical Modeling of the Absorption and Magnetic Circular Dichroism Spectra of Monomeric and Dimeric Zinc Phthalocyanine Cation-Radical. *Inorg. Chem.* **2019**, *58*, 14120−14135.
(62) Mack, J.; Stillman, M. J. Assignment of the optical spectra of metal phthalocyanines through spectral band deconvolution analysis and ZINDO calculations. *Coord. Chem. Rev.* **2001**, *219−221*, 993−1032.
(63) Stillman, M. Formation and electronic properties of ring-oxidized and ring-reduced radical species of the phthalocyanines and porphyrins. *J. Porphyrins Phthalocyanines* **2000**, *4*, 374−376.
(64) Ough, E.; Gasyna, Z.; Stillman, M. J. Photochemical, electrochemical, and chemical formation of the π-cation-radical species of magnesium phthalocyanine. Analysis of the absorption and MCD spectra of $[MgPc(-1)]^{+}$. *Inorg. Chem.* **1991**, *30*, 2301−2310.
(65) Ough, E. A.; Stillman, M. J. Analysis of the absorption and magnetic circular dichroism spectra of low spin (S = 1/2) iron(III) phthalocyanine. *Inorg. Chem.* **1995**, *34*, 4317−4325.
(66) Ough, E. A. Metal and Ring Oxidation in Metallophthalocyanines. Ph.D. Thesis, University of Western Ontario: Canada, 1993; 232 p. https://ir.lib.uwo.ca/cgi/viewcontent.cgi?article=3233&context=digitizedtheses.
(67) Nevonen, D. E.; Ferch, L. S.; Schrage, B. R.; Nemykin, V. N. Charge-Transfer Spectroscopy of Bisaxially Coordinated Iron(II) Phthalocyanines through the Prism of the Lever's EL Parameters Scale, MCD Spectroscopy, and TDDFT Calculations. *Inorg. Chem.* **2022**, *61*, 8250−8266.
(68) Nemykin, V. N.; Purchel, A. A.; Spaeth, A. D.; Barybin, M. V. Probing the Electronic Properties of a Trinuclear Molecular Wire Involving Isocyanoferrocene and Iron(II) Phthalocyanine Motifs. *Inorg. Chem.* **2013**, *52*, 11004−11012.
(69) Nemykin, V. N.; Kobayashi, N.; Chernii, V. Y.; Belsky, V. K. Mossbauer, crystallographic, and density functional theoretical investigation of the electronic structure of bis-ligated low-spin iron(II) phthalocyanines. *Eur. J. Inorg. Chem.* **2001**, 733−743.
(70) Ercolani, C.; Monacelli, F.; Dzugan, S.; Goedken, V. L.; Pennesi, G.; Rossi, G. X-ray crystal structure of μ-oxo-bis[(1-methylimidazole)phthalocyaninatoiron(III)] and comments on the molecular structure and chemistry of oxo-bridged iron phthalocyaninate dimers. *J. Chem. Soc., Dalton Trans.* **1991**, 1309−1315.
(71) Chilton, N. F.; Anderson, R. P.; Turner, L. D.; Soncini, A.; Murray, K. S. PHI: a powerful new program for the analysis of anisotropic monomeric and exchange-coupled polynuclear d- and f-block complexes. *J. Comput. Chem.* **2013**, *34*, 1164−1175.
(72) Bottomley, L. A.; Ercolani, C.; Gorce, J. N.; Pennesi, G.; Rossi, G. Spectroelectrochemistry of (μ-oxo)bis[phthalocyaninato)iron-(III)]. *Inorg. Chem.* **1986**, *25*, 2338−2342.
(73) Nemykin, V. N.; Nevonen, D. E.; Osterloh, W. R.; Ferch, L. S.; Harrison, L. A.; Marx, B. S.; Kadish, K. M. Application of Lever's E-L Parameter Scale toward Fe(II)/Fe(III) versus Pc(2-)/Pc(1-) Oxidation Process Crossover Point in Axially Coordinated Iron(II) Phthalocyanine Complexes. *Inorg. Chem.* **2021**, *60*, 16626−16644.
(74) Lin, M.-J.; Wang, J.-D.; Chen, N.-S.; Huang, J.-L. Different conformations of phthalocyanine skeletons in a structure of l-oxo-bis(phthalocyaninato)iron with asymmetry coordination. *Inorg. Chem. Commun.* **2005**, *8*, 900−902.
(75) Bouvet, M.; Gaudillat, P.; Suisse, J.-M. Lanthanide macrocyclic complexes: from molecules to materials and from materials to devices. *J. Porphyrins Phthalocyanines* **2013**, *17*, 628−635.
(76) Pushkarev, V. E.; Tolbin, A. Yu.; Zhurkin, F. E.; Borisova, N. E.; Trashin, S. A.; Tomilova, L. G.; Zefirov, N. S. Sandwich Double-Decker Lanthanide(III) "Intracavity" Complexes Based on Clamshell-Type Phthalocyanine Ligands: Synthesis, Spectral, Electrochemical, and Spectroelectrochemical Investigations. *Chem.—Eur. J.* **2012**, *18*, 9046−9055.
(77) Ishikawa, N.; Kaizu, Y. Synthetic, spectroscopic and theoretical study of novel supramolecular structures composed of lanthanide phthalocyanine double-decker complexes. *Coord. Chem. Rev.* **2002**, *226*, 93−101.
(78) Ishikawa, N.; Kaizu, Y. Axially polarized NIR absorption bands in electron-deficient lanthanide phthalocyanine dimers and trimers. *J. Porphyrins Phthalocyanines* **1999**, *3*, 514−521.
(79) Dmitrieva, E.; Sturtz, B. W.; Yang, Y.; Zhang, P.; Dunsch, L.; Kenney, M. E. An in situ spectroelectrochemical study of the dimeric phthalocyanines $[(SiPc)_2O][OSiHx_3]_2$, $[(SiPc)_2O][OSiHx_3]_2^{\bullet+}$, and $[(SiPc)_2O][OSiHx_3]_2^{2+}$. *Electrochem. Commun.* **2021**, *128*, No. 107048.
(80) Matassa, R.; Ballirano, P.; Donzello, M. P.; Ercolani, C.; Sadun, C.; Caminiti, R. A nanostructured polymorph of μ-oxobis-(phthalocyaninatoiron(III)) studied by Angular and Energy Dispersive X-ray Diffraction. *Nano* **2007**, *2*, 121−128.
(81) Gürek, A. G.; Basova, T.; Luneau, D.; Lebrun, C.; Kol'tsov, E.; Hassan, A. K.; Ahsen, V. Synthesis, Structure, and Spectroscopic and Magnetic Properties of Mesomorphic Octakis(hexylthio)-Substituted Phthalocyanine Rare-Earth Metal Sandwich Complexes. *Inorg. Chem.* **2006**, *45*, 1667−1676.
(82) Zhu, P.; Pan, N.; Li, R.; Dou, J.; Zhang, Y.; Cheng, D. Y. Y.; Wang, D.; Ng, D. K. P.; Jiang, J. Electron-donating alkoxy-group-driven synthesis of heteroleptic tris(phthalocyaninato)lanthanide(III) triple-deckers with symmetrical molecular structure. *Chem.—Eur. J.* **2005**, *11*, 1425−1432.
(83) Haghighi, M. S.; Franken, A.; Homborg, H. Crystal-chemical analysis of the stereochemistry of the cations and anions in bis(triphenylphosphine)iminium di(phthalocyaninato)metalates of the rare earth elements, $(PNP)[Ln(Pc^{2-})_2]\cdot xH_2O$ (Ln = La, Gd, Tm; $x \leq 0.5$). *Z. Naturforsch., B* **1994**, *49*, 812−820.
(84) Pushkarev, V. E.; Tomilova, L. G.; Nemykin, V. N. Historic overview and new developments in synthetic methods for preparation of the rare-earth tetrapyrrolic complexes. *Coord. Chem. Rev.* **2016**, *319*, 110−179.

https://doi.org/10.1021/acs.inorgchem.3c00897
Inorg. Chem. 2023, 62, 10203−10220

(85) Gouterman, M. Effects of substitution on the absorption spectra of porphin. *J. Chem. Phys.* **1959**, *30*, 1139−1161.
(86) Gouterman, M. Spectra of porphyrins. *J. Mol. Spectrosc.* **1961**, *6*, 138−163.
(87) Gouterman, M.; Wagniere, G.; Snyder, L. C. Spectra of porphyrins. II. Four-orbital model. *J. Mol. Spectrosc.* **1963**, *11*, 108−127.
(88) Kasha, M.; Rawls, H. R.; El-Bayoumi, M. A. Exciton model in molecular spectroscopy. *Pure Appl. Chem.* **1965**, *11*, 371−392.
(89) Kobayashi, N.; Muranaka, A.; Mack, J.*Circular Dichroism and Magnetic Circular Dichroism Spectroscopy for Organic Chemists*; RSC, 2012; Vol. *Chapter 1*, pp 1−41.
(90) Moore, B., II; Autschbach, J. Density Functional Study of Tetraphenylporphyrin Long-Range Exciton Coupling. *ChemistryOpen* **2012**, *1*, 184−194.
(91) Vogt, L. H., Jr.; Zalkin, A.; Templeton, D. H. The crystal and molecular structure of phthalocyanatopyridine-manganese(III)-u-oxo-phthalocyanatopyridine-manganese(III) dipyridinate. *Inorg. Chem.* **1967**, *6*, 1725−1730.
(92) Dirk, C. W.; Inabe, T.; Schoch, K. F., Jr.; Marks, T. J. Cofacial assembly of partially oxidized metallamacrocycles as an approach to controlling lattice architecture in low-dimensional molecular solids. Chemical and architectural properties of the "face-to-face" polymers [M(phthalocyaninato)O]n, where M = Si, Ge, and Sn. *J. Am. Chem. Soc.* **1983**, *105*, 1539−1550.
(93) Zhao, Z.; Cammidge, A. N.; Hughes, D. L.; Cook, M. J. Modular Face-to-Face Assembly of Multichromophore Arrays that Absorb Across the Complete UV-Visible Spectrum and into the Near-IR. *Org. Lett.* **2010**, *12*, 5138−5141.
(94) Basova, T. V.; Kiselev, V. G.; Latteyer, F.; Peisert, H.; Chasse, T. Molecular organization in the thin films of gallium(III) phthalocyanine chloride and its μ-(oxo)dimer: Optical spectroscopy and XPS study. *Appl. Surf. Sci.* **2014**, *322*, 242−248.
(95) Lapkina, L. A.; Larchenko, V. E.; Kirakosyan, G. A.; Tsivadze, A. Yu.; Troyanov, S. I.; Gorbunova, Y. G. Cation-Induced Dimerization of Crown-Substituted Phthalocyanines by Complexation with Rubidium Nicotinate As Revealed by X-ray Structural Data. *Inorg. Chem.* **2018**, *57*, 82−85.
(96) Ohno, O.; Ishikawa, N.; Matsuzawa, H.; Kaizu, Y.; Kobayashi, H. Exciton coupling in bis(phthalocyaninato)tin(IV). *J. Phys. Chem. A* **1989**, *93*, 1713−1718.
(97) Ishikawa, N.; Ohno, O.; Kaizu, Y.; Kobayashi, H. Localized orbital study on the electronic structure of phthalocyanine dimers. *J. Phys. Chem. A* **1992**, *96*, 8832−8839.
(98) Ishikawa, N.; Kaizu, Y. Exciton coupling and charge resonance in the lowest excited states of lutetium phthalocyanine dimer and trimer. *Chem. Phys. Lett.* **1994**, *228*, 625−632.
(99) Ishikawa, N. Electronic structures and spectral properties of double- and triple-decker phthalocyanine complexes in a localized molecular orbital view. *J. Porphyrins Phthalocyanines* **2001**, *5*, 87−101.
(100) Kobayashi, N.; Furuya, F.; Yug, G.-C.; Wakita, H.; Yokomizo, M.; Ishikawa, N. Synthesis and characterization of phthalocyanines with direct Si-Si linkages. *Chem.—Eur. J.* **2002**, *8*, 1474−1484.
(101) Ghosh, R.; Spano, F. C. Excitons and Polarons in Organic Materials. *Acc. Chem. Res.* **2020**, *53*, 2201−2211.
(102) Hestand, N. J.; Spano, F. C. Expanded Theory of H- and J-Molecular Aggregates: Effects of Vibronic Coupling and Intermolecular Charge Transfer. *Chem. Rev.* **2018**, *118*, 7069−7163.
(103) Hestand, N. J.; Spano, F. C. Molecular Aggregate Photophysics beyond the Kasha Model: Novel Design Principles for Organic Materials. *Acc. Chem. Res.* **2017**, *50*, 341−350.
(104) Bialas, D.; Zhong, C.; Wurthner, F.; Spano, F. C. Essential States Model for Merocyanine Dye Stacks: Bridging Electronic and Optical Absorption Properties. *J. Phys. Chem. C* **2019**, *123*, 18654−18664.
(105) Chang, X.; Balooch Qarai, M.; Spano, F. C. Intermolecular Charge Transfer in H- and J-Aggregates of Donor-Acceptor-Donor Chromophores: The Curious Case of Bithiophene-DPP. *J. Phys. Chem. C* **2022**, *126*, 18784−18795.
(106) Chang, X.; Balooch Qarai, M.; Spano, F. C. HJ-aggregates of donor-acceptor-donor oligomers and polymers. *J. Chem. Phys.* **2021**, *155*, No. 034905.
(107) O'Connor, C. J. In *Progress in Inorganic Chemistry*; Lippard, S. J., Ed.; Wiley & Sons, 1982; Vol. *29*, pp 203−283.
(108) Frisch, M. J.; Trucks, G. W.; Schlegel, H. B.; Scuseria, G. E.; Robb, M. A.; Cheeseman, J. R.; Scalmani, G.; Barone, V.; Petersson, G. A.; Nakatsuji, H.; Li, X.; Caricato, M.; Marenich, A. V.; Bloino, J.; Janesko, B. G.; Gomperts, R.; Mennucci, B.; Hratchian, H. P.; Ortiz, J. V.; Izmaylov, A. F.; Sonnenberg, J. L.; Williams-Young, D.; Ding, F.; Lipparini, F.; Egidi, F.; Goings, J.; Peng, B.; Petrone, A.; Henderson, T.; Ranasinghe, D.; Zakrzewski, V. G.; Gao, J.; Rega, N.; Zheng, G.; Liang, W.; Hada, M.; Ehara, M.; Toyota, K.; Fukuda, R.; Hasegawa, J.; Ishida, M.; Nakajima, T.; Honda, Y.; Kitao, O.; Nakai, H.; Vreven, T.; Throssell, K.; Montgomery, J. A., Jr.; Peralta, J. E.; Ogliaro, F.; Bearpark, M. J.; Heyd, J. J.; Brothers, E. N.; Kudin, K. N.; Staroverov, V. N.; Keith, T. A.; Kobayashi, R.; Normand, J.; Raghavachari, K.; Rendell, A. P.; Burant, J. C.; Iyengar, S. S.; Tomasi, J.; Cossi, M.; Millam, J. M.; Klene, M.; Adamo, C.; Cammi, R.; Ochterski, J. W.; Martin, R. L.; Morokuma, K.; Farkas, O.; Foresman, J. B.; Fox, D. J. *Gaussian 16*, revision B.01; Gaussian, Inc.: Wallingford, CT, 2016.
(109) Henderson, T. M.; Izmaylov, A. F.; Scuseria, G. E.; Savin, A. Assessment of a Middle Range Hybrid Functional. *J. Chem. Theory Comput.* **2008**, *4*, 1254−1262.
(110) Wachters, A. J. H. Gaussian Basis Set for Molecular Wavefunctions Containing Third-Row Atoms. *J. Chem. Phys.* **1970**, *52*, 1033−1036.
(111) McLean, A. D.; Chandler, G. S. Contracted Gaussian basis sets for molecular calculations. 1. Second row atoms, Z = 11-18. *J. Chem. Phys.* **1980**, *72*, 5639−5648.
(112) Becke, A. D. Density-functional exchange-energy approximation with correct asymptotic behaviour. *Phys. Rev. A* **1988**, *38*, 3098−3100.
(113) Perdew, J. P. Density-functional approximation for the correlation energy of the inhomogeneous electron gas. *Phys. Rev. B* **1986**, *33*, 8822−8824.
(114) Grimme, S.; Antony, J.; Ehrlich, S.; Krieg, H. A Consistent and Accurate *ab initio* Parametrization of Density Functional Dispersion Correction (DFT-D) for the 94 Elements H-Pu. *J. Chem. Phys.* **2010**, *132*, No. 154104.
(115) Grimme, S.; Ehrlich, S.; Goerigk, L. Effect of the Damping Function in Dispersion Corrected Density Functional Theory. *J. Comput. Chem.* **2011**, *32*, 1456−1465.
(116) Boese, A. D.; Martin, J. M. L. Development of density functionals for thermochemical kinetics. *J. Chem. Phys.* **2004**, *121*, 3405−3416.
(117) Becke, A. D. Density-Functional Thermochemistry. V. Systematic Optimization of Exchange-Correlation Functionals. *J. Chem. Phys.* **1997**, *107*, 8554−8560.
(118) Becke, A. D. Density-functional thermochemistry. III. The role of exact exchange. *J. Chem. Phys.* **1993**, *98*, 5648−5652.
(119) Xu, X.; Goddard, W. A., III. The X3LYP Extended Density Functional for Accurate Descriptions of Nonbond Interactions, Spin States, and Thermochemical Properties. *Proc. Natl. Acad. Sci. U.S.A.* **2004**, *101*, 2673−2677.
(120) Austin, A.; Petersson, G.; Frisch, M. J.; Dobek, F. J.; Scalmani, G.; Throssell, K. A density functional with spherical atom dispersion terms. *J. Chem. Theory Comput.* **2012**, *8*, 4989−5007.
(121) Ernzerhof, M.; Perdew, J. P. Generalized gradient approximation to the angle- and system-averaged exchange hole. *J. Chem. Phys.* **1998**, *109*, 3313−3320.
(122) Henderson, T. M.; Izmaylov, A. F.; Scalmani, G.; Scuseria, G. E. Can short-range hybrids describe long-range-dependent properties? *J. Chem. Phys.* **2009**, *131*, No. 044108.
(123) Heyd, J.; Scuseria, G. E.; Ernzerhof, M. Hybrid Functionals Based on a Screened Coulomb Potential. *J. Chem. Phys.* **2003**, *118*, 8207−8215.

https://doi.org/10.1021/acs.inorgchem.3c00897
Inorg. Chem. 2023, 62, 10203−10220

(124) Schmider, H. L.; Becke, A. D. Optimized Density Functionals from the Extended G2 Test Set. *J. Chem. Phys.* **1998**, *108*, 9624−9631.
(125) Hamprecht, F. A.; Cohen, A.; Tozer, D. J.; Handy, N. C. Development and Assessment of New Exchange-Correlation Functionals. *J. Chem. Phys.* **1998**, *109*, 6264−6271.
(126) Wilson, P. J.; Bradley, T. J.; Tozer, D. J. Hybrid Exchange-Correlation Functional Determined from Thermochemical Data and *ab initio* Potentials. *J. Chem. Phys.* **2001**, *115*, 9233−9242.
(127) Zhao, Y.; Truhlar, D. G. The M06 Suite of Density Functionals for Main Group Thermochemistry, Thermochemical Kinetics, Noncovalent Interactions, Excited States, and Transition Elements: Two New Functionals and Systematic Testing of Four M06 Functionals and Twelve Other Functionals. *Theor. Chem. Acc.* **2008**, *120*, 215−241.
(128) Zhao, Y.; Schultz, N. E.; Truhlar, D. G. Exchange-Correlation Functionals with Broad Accuracy for Metallic and Nonmetallic Compounds, Kinetics, and Noncovalent Interactions. *J. Chem. Phys.* **2005**, *123*, No. 161103.
(129) Peverati, R.; Truhlar, D. G. Exchange-Correlation Functional with Good Accuracy for Both Structural and Energetic Properties while Depending Only on the Density and Its Gradient. *J. Chem. Theory Comput.* **2012**, *8*, 2310−2319.
(130) Peverati, R.; Truhlar, D. G. Screened-Exchange Density Functionals with Broad Accuracy for Chemistry and Solid-State Physics. *Phys. Chem. Chem. Phys.* **2012**, *14*, 16187−16191.
(131) Peverati, R.; Truhlar, D. G. An Improved and Broadly Accurate Local Approximation to the Exchange-Correlation Density Functional: The MN12-L Functional for Electronic Structure Calculations in Chemistry and Physics. *Phys. Chem. Chem. Phys.* **2012**, *14*, 13171−13174.
(132) Chai, J. D.; Head-Gordon, M. Systematic Optimization of Long-Range Corrected Hybrid Density Functionals. *J. Chem. Phys.* **2008**, *128*, No. 084106.
(133) Yanai, T.; Tew, D.; Handy, N. A New Hybrid Exchange-Correlation Functional Using the Coulomb-Attenuating Method (CAM-B3LYP). *Chem. Phys. Lett.* **2004**, *393*, 51−57.
(134) Chai, J. D.; Head-Gordon, M. Long-Range Corrected Hybrid Density Functionals with Damped Atom-Atom Dispersion Corrections. *Phys. Chem. Chem. Phys.* **2008**, *10*, 6615−6620.
(135) Peverati, R.; Zhao, Y.; Truhlar, D. G. Generalized Gradient Approximation that Recovers the Second-Order Density-Gradient Expansion with Optimized Across-the-board Performance. *J. Phys. Chem. Lett.* **2011**, *2*, 1991−1997.
(136) Tomasi, J.; Mennucci, B.; Cammi, R. Quantum mechanical continuum solvation models. *Chem. Rev.* **2005**, *105*, 2999−3093.
(137) Tenderholt, A. L. *QMForge*, version 2.1; Standord University: Stanford, CA, 2011. https://qmforge.net/.
(138) Yamanaka, S.; Kawakami, T.; Nagao, H.; Yamaguchi, K. Effective exchange integrals for open-shell species by density functional methods. *Chem. Phys. Lett.* **1994**, *231*, 25−33.
(139) Pantazis, D. A.; Krewald, V.; Orio, M.; Neese, F. Theoretical magnetochemistry of dinuclear manganese complexes: broken symmetry density functional theory investigation on the influence of bridging motifs on structure and magnetism. *Dalton Trans.* **2010**, *39*, 4959−4967.
(140) Tiedemann, M. T.; Stillman, M. J. Application of magnetic circular dichroism spectroscopy to porphyrins, phthalocyanines and hemes. *J. Porphyrins Phthalocyanines* **2011**, *15*, 1134−1149.
(141) Stillman, M. J. Theoretical Aspects of the Optical Spectroscopy of Porphyrinoids. In *Handbook of Porphyrin Science*; Kadish, K. M.; Smith, K. M.; Guilard, R., Eds.; World Scientific, 2011; Vol. *14*, pp 461−524.

https://doi.org/10.1021/acs.inorgchem.3c00897
Inorg. Chem. 2023, 62, 10203−10220